

UC San Diego

UC San Diego Previously Published Works

Title

Unfolded protein response IRE1/XBP1 signaling is required for healthy mammalian brain aging

Permalink

<https://escholarship.org/uc/item/4bk3h3sk>

Journal

The EMBO Journal, 41(22)

ISSN

0261-4189

Authors

Cabral-Miranda, Felipe

Tamburini, Giovanni

Martinez, Gabriela

et al.

Publication Date











2022-11-17

DOI

10.15252/emj.2022111952

Peer reviewed

# Unfolded protein response IRE1/XBP1 signaling is required for healthy mammalian brain aging

Felipe Cabral-Miranda<sup>1,2,3,4</sup>, Giovanni Tamburini<sup>1,2,3</sup>, Gabriela Martinez<sup>1,2,3</sup>, Alvaro O Ardiles<sup>5,6</sup> , Danilo B Medinas<sup>1,2,3</sup> , Yannis Gerakis<sup>1,2,3</sup>, Mei-Li Diaz Hung<sup>1,2,3</sup>, René Vidal<sup>1,2,7</sup>, Matias Fuentealba<sup>1,2,3</sup>, Tim Miedema<sup>1,2,3</sup> , Claudia Duran-Aniotz<sup>1,2,3</sup>, Javier Diaz<sup>1,2,3</sup>, Cristobal Ibaceta-Gonzalez<sup>5</sup>, Carleen M Sabusap<sup>8</sup>, Francisca Bermedo-Garcia<sup>9</sup>, Paula Mujica<sup>6</sup>, Stuart Adamson<sup>10</sup> , Kaitlyn Vitangcol<sup>10</sup>, Hernan Huerta<sup>7</sup> , Xu Zhang<sup>11</sup>, Tomohiro Nakamura<sup>11</sup>, Sergio Pablo Sardi<sup>12</sup> , Stuart A Lipton<sup>11,13</sup> , Brian K Kennedy<sup>10,14</sup>, Juan Pablo Henriquez<sup>9</sup>, J Cesar Cárdenas<sup>1,7,10</sup>, Lars Plate<sup>8</sup> , Adrian G Palacios<sup>5</sup>  & Claudio Hetz<sup>1,2,3,10,\*</sup> 

## Abstract

Aging is a major risk factor to develop neurodegenerative diseases and is associated with decreased buffering capacity of the proteostasis network. We investigated the significance of the unfolded protein response (UPR), a major signaling pathway activated to cope with endoplasmic reticulum (ER) stress, in the functional deterioration of the mammalian brain during aging. We report that genetic disruption of the ER stress sensor IRE1 accelerated age-related cognitive decline. In mouse models, overexpressing an active form of the UPR transcription factor XBP1 restored synaptic and cognitive function, in addition to reducing cell senescence. Proteomic profiling of hippocampal tissue showed that XBP1 expression significantly restore changes associated with aging, including factors involved in synaptic function and pathways linked to neurodegenerative diseases. The genes modified by XBP1 in the aged hippocampus were also altered. Collectively, our results demonstrate that strategies to manipulate the UPR in mammals may help sustain healthy brain aging.

**Keywords** aging brain; ER stress; proteostasis; UPR; XBP1s

**Subject Categories** Molecular Biology of Disease; Neuroscience; Translation & Protein Quality

DOI 10.15252/embj.2022111952 | Received 22 June 2022 | Revised 9 September 2022 | Accepted 16 September 2022 | Published online 31 October 2022

The EMBO Journal (2022) 41: e111952

## Introduction

Normal aging is associated with a progressive cognitive impairment and also represents the major risk factor for developing dementia and neurodegenerative disorders (Morrison & Baxter, 2012). Worldwide, around 50 million people have dementia, and nearly 10 million new cases are reported every year, constituting a major cause of disability and dependency among older people worldwide (WHO, 2020). Dementia represents a progressive syndrome with substantial impairment in cognitive function beyond what might be expected from normal aging and is associated with various neurodegenerative disorders such as Alzheimer's disease (AD), Parkinson's disease (PD)/Lewy body dementia (LBD), and Frontotemporal dementia (FTD).

Decades of research have defined the hallmarks of aging, underscoring the biological processes that determine when and how organisms age, ultimately regulating health span and life span across species (López-Otín *et al*, 2013; Kennedy *et al*, 2014). Brain

1 Center for Geroscience, Brain Health and Metabolism, Santiago, Chile

2 Biomedical Neuroscience Institute, Faculty of Medicine, University of Chile, Santiago, Chile

3 Program of Cellular and Molecular Biology, Institute of Biomedical Sciences, Faculty of Medicine, University of Chile, Santiago, Chile

4 Instituto de Ciências Biomédicas, Universidade Federal do Rio de Janeiro, Rio de Janeiro, Brazil

5 Centro Interdisciplinario de Neurociencia de Valparaíso, Universidad de Valparaíso, Valparaíso, Chile

6 Centro de Neurología Traslacional, Escuela de Medicina, Universidad de Valparaíso, Valparaíso, Chile

7 Center for Integrative Biology, Universidad Mayor, Santiago, Chile

8 Departments of Chemistry and Biological Sciences, Vanderbilt University, Nashville, TN, USA

9 Department of Cell Biology, Center for Advanced Microscopy (CMA BioBio), Universidad de Concepción, Concepción, Chile

10 Buck Institute for Research on Aging, Novato, CA, USA

11 Department of Molecular Medicine and Neurodegeneration New Medicines Center, The Scripps Research Institute, La Jolla, CA, USA

12 Rare and Neurological Diseases Therapeutic Area, Sanofi, Framingham, MA, USA

13 Department of Neurosciences, School of Medicine, University of California, San Diego, La Jolla, CA, USA

14 Healthy Longevity Translational Research Programme, Yong Loo Lin School of Medicine, National University of Singapore; Centre for Healthy Longevity, National University Health System; Departments of Biochemistry and Physiology, Yong Loo Lin School of Medicine, National University of Singapore, Singapore, Singapore

\*Corresponding author. Tel: +56229786506; E-mail: chetz@uchile.cl or chetz@buckinstitute.org

aging itself, like the major neurodegenerative diseases, can be associated with abnormal deposition of protein aggregates in the brain (Soto & Pritzkow, 2018). Consistent with this idea, the pathways that sustain proteome homeostasis (proteostasis) are substantially altered in aged organisms, a phenomenon considered a pillar of the aging process<sup>4</sup>. Proteostasis is maintained by the dynamic integration of pathways that mediate the synthesis, folding, degradation, quality control, trafficking, and targeting of proteins (Morimoto & Cuervo, 2014). A central site of proteostatic processes is the endoplasmic reticulum (ER), the main subcellular compartment involved in protein folding and secretion. Several factors regulate and ensure folding and quality control of newly synthesized proteins at the ER, including protein chaperones and other cofactors that also mediate degradation of unfolded proteins and prevent formation of protein aggregates with cytotoxic potential (Walter & Ron, 2011). Abnormal levels of misfolded proteins in the ER lumen result in a cellular state known as “ER stress,” which, in turn, engages an adaptive reaction to restore proteostasis and sustain cell function—this process is known as the unfolded protein response (UPR) (Walter & Ron, 2011). Studies in simple model organisms have demonstrated that the activity of the UPR is compromised during aging (Taylor & Hetz, 2020), ultimately impacting health span and life span.

Three main pathways that sense cell stress encompass the UPR—these are comprised of inositol-requiring enzyme-1 (IRE1) alpha and beta, PKR-like ER kinase (PERK), and activating transcription factor 6 (ATF6) alpha and beta (Hetz et al, 2020). IRE1 is an ER-located kinase and RNase that upon activation catalyzes unconventional splicing of mRNA encoding X-box binding protein-1 (XBP1), eliminating a 26-nucleotide intron (Walter & Ron, 2011). This processing event results in the expression of an active transcription factor called XBP1s that controls expression of chaperones and other mediators of protein quality control mechanisms (Hetz et al, 2020). In response to ER stress, PERK phosphorylates eukaryotic translation initiation factor 2A (eIF2 $\alpha$ ), inhibiting global protein translation but paradoxically upregulating the translation of specific mRNAs such as activated transcription factor-4 (*Atf4*) (Costa-Mattioli & Walter, 2020). ATF4 regulates the expression of ER chaperones and genes related to apoptosis, protein synthesis, and redox control, including C/EBP-homologous protein (CHOP/GADD153) (Costa-Mattioli & Walter, 2020). Finally, following ER stress, ATF6 reaches the Golgi apparatus, where it is processed to release a cytosolic fragment (ATF6f) that acts as a transcription factor to regulate expression of genes involved in ER-associated degradation (ERAD) and folding (Hetz et al, 2020).

Besides its well-characterized function as a stress mitigation pathway, various UPR mediators have been shown to exert other important physiological roles in the brain. For example, in mammals, UPR components display important functions that affect brain development, synaptic plasticity, and metabolic control (Godin et al, 2016; Martínez et al, 2018). Expression of XBP1 in the hippocampus regulates synaptic plasticity and memory-related processes, partially mediated by transcriptional control of brain-derived neurotrophic factor (BDNF) (Martínez et al, 2016). The complexity of synaptic architecture and its dynamic regulation highlight the requirement for maintenance of proteostasis at the level of the secretory pathway during the organismal life span to sustain normal brain function (Hanus & Ehlers, 2016). Subtle structural and functional alterations in synapses are the main drivers of age-related

cognitive decline (Morrison & Baxter, 2012), but the molecular mechanisms dictating these perturbations remain elusive although they have been postulated to be related to proteostasis.

In those lines, it is reasonable to hypothesize that UPR, and particularly, the IRE-XBP1s pathway may impact the aging process in the mammalian brain (Taylor, 2016). Accordingly, correlative studies in mammals have demonstrated impaired UPR signaling in brain tissue (Gavilán et al, 2006; Hussain & Ramaiah, 2007; Naidoo et al, 2008; Naidoo et al, 2011; Brown et al, 2014; Taylor, 2016; Martínez et al, 2017, for review), but the significance of such disruption has only recently been evaluated by manipulating the PERK/eIF2 $\alpha$  signaling branch eIF2 $\alpha$  (Sharma et al, 2018; Krukowski et al, 2020; Hafycz et al, 2022). Notably, studies in invertebrates indicated that overexpression of XBP1s in neurons extends life span and is associated with activation of the UPR in peripheral organs through a cell-nonautonomous mechanism (Taylor & Dillin, 2013). Importantly, UPR alterations have also been described in human tissue (Hetz, 2021).

Here, we investigated the functional contribution of the UPR to age-associated cognitive impairment in the mammalian brain. Accordingly, we combined a series of genetic strategies to manipulate the IRE1/XBP1 pathway in the brain coupled with assessments of cognitive function, electrophysiological properties, structural attributes, and protein expression. Our results indicate that ablation of IRE1 function accelerates age-dependent cognitive decline, whereas artificial bolstering of XBP1s levels is sufficient to prevent or even revert cognitive deterioration, while maintaining the integrity of synaptic transmission and diminishing the natural accumulation of senescent cells.

## Results

### The ER proteostasis network is altered in elderly mammals during normal brain aging or dementia

Initially, to study possible contributions of the UPR to age-associated cognitive decline in humans, we analyzed RNA sequencing data from the hippocampus of normal subjects as well as those diagnosed with dementia in a unique aged population-based cohort from the Adult Changes in Thought (ACT) study (<http://aging.brain-map.org>). Remarkably, an unbiased functional enrichment analysis of differentially expressed genes (DEGs) in demented patients revealed that “unfolded protein binding and processing” are the most altered biological functions (Fig 1A). Moreover, XBP1 was predicted as one of the possible transcription factors driving such alterations in the proteostasis network (Fig 1A; Dataset EV1 for a complete analysis). In addition, chaperones accounted for the most altered genes in patients with dementia in the dataset analyzed (Fig 1B, Table 1), while some classical UPR mediators were not altered (Fig EV1A).

To determine the age-related capacity of the mammalian brain to engage the UPR, we treated young, middle-aged, and aged mice with intraperitoneal injection of tunicamycin, a well-established pharmacological inducer of ER stress (Medinas et al, 2018; Fig 1C). This regimen was used to test whether activation of the UPR is altered by stress at various time points during aging. Tunicamycin is known to induce a high level of ER stress, thus facilitating measurement of UPR signaling. We monitored mRNA levels of *Xbp1s*, *Hspa5* (*Bip*/

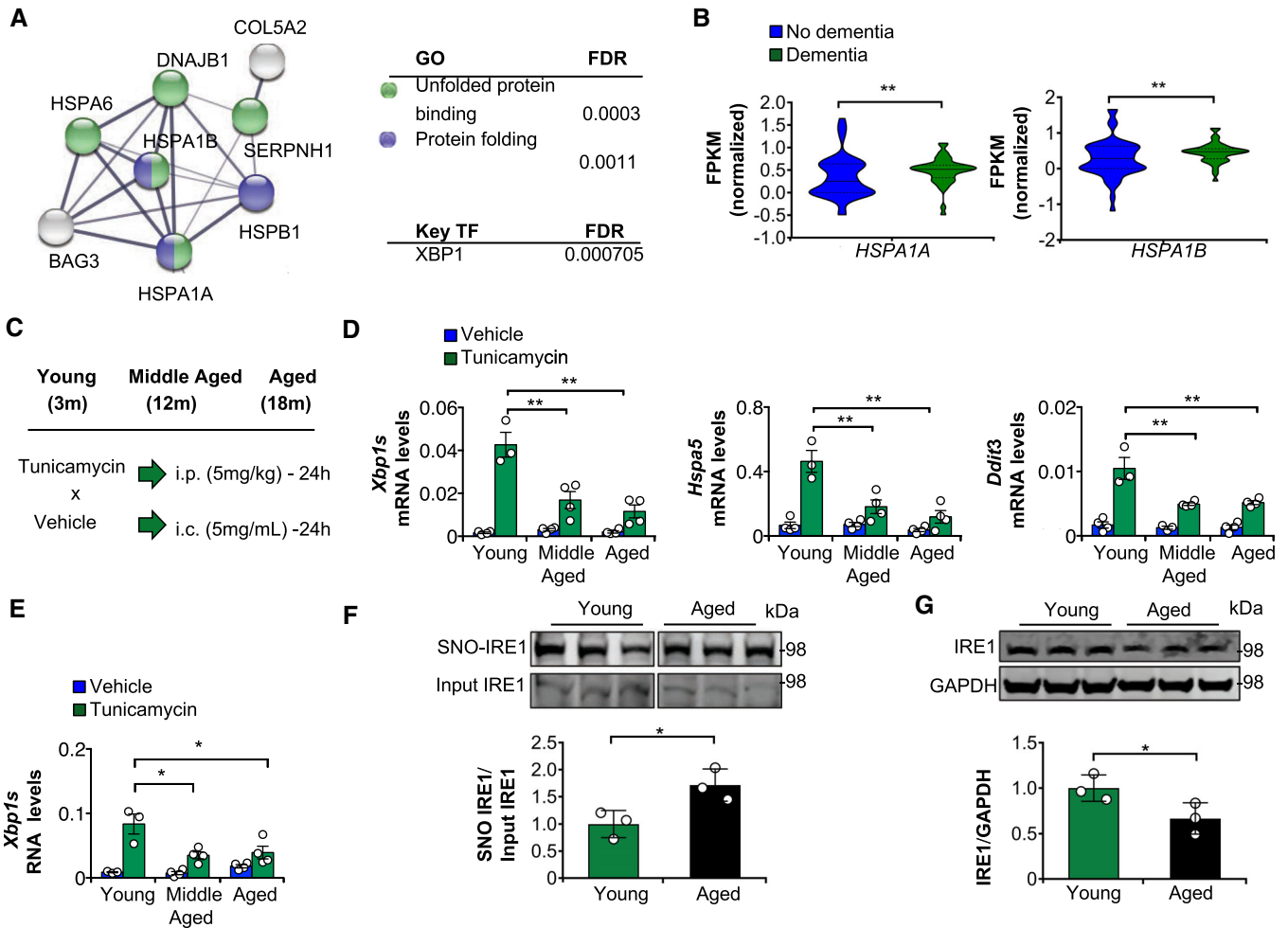


**Figure 1. Impaired UPR activation in the mammalian aged brain.**

**A** Functional enrichment analysis of altered genes in an elderly cohort of patients diagnosed with dementia versus non-demented. GO, gene ontology; FDR, false discovery rate; Key TF, key transcription factor in TRRUST database.

**B** Violin plots displaying RNA-seq readings by FPKM (normalized Fragments Per Kilobase Million) of chaperones HSPA1A and HSPA1B of human hippocampus samples of demented patients and controls ( $n = 49, 42$ ; unpaired Kolmogorov–Smirnov test; continuous lines: median; dashed lines: quartiles).

**C** Pharmacological models of ER stress induction. Animals of indicated ages were injected with ER stress inducer tunicamycin through intraperitoneal (i.p.) injection. After 24 h, the brain was dissected to measure UPR signaling using RT-PCR. Alternatively, animals received tunicamycin intracerebrally (i.c.) directly into the hippocampus using stereotaxic injection.

**D** Mean and SEM of mRNA levels of Xbp1s, Bip/Hspa5 and Chop/Ddit3 were determined in dissected hippocampus of i.p. treated mice by quantitative RT-PCR. ( $n = 3-4$  animals/group. One-way ANOVA followed by Tukey's post-test compared tunicamycin treated groups).

**E** Animals received bilateral intrahippocampal injections of 2  $\mu$ l tunicamycin (5 mg/ml) or vehicle for 24 h. Graphs indicate mean and s.e.m. of Xbp1s mRNA levels in the hippocampus ( $n = 3-4$  animals/group. One-way ANOVA followed by Tukey's post-test compared tunicamycin treated groups).

**F, G** Mean and SEM of relative levels of S-nitrosylated IRE1 (**F**) and total IRE1 (**G**) in brains from young and aged mice. Histograms show relative levels of SNO-IRE1/input IRE1 measured by biotin-switch assay and total IRE1/GAPDH quantified by densitometry on standard immunoblots for young (3-month-old) versus aged (24-month-old) mouse brains ( $n = 3$ , unpaired Student's *t*-test). Data information: All graphs indicate *P*-values with the following legend: \**P* < 0.05; \*\**P* < 0.01.

Source data are available online for this figure.

Grp78), and *Ddit3* (*Chop*) in the hippocampus, in addition to cerebral cortex and cerebellum. Remarkably, the capacity to induce *Xbp1s* was significantly attenuated in the hippocampus of middle-aged and aged animals compared with young animals following experimental ER stress (Fig 1D, left). The UPR mediators *Ddit3* and *Hspa5* manifested similar findings (Fig 1D, middle and right), whereas other markers such as *Atf3* and *Pdia3* did not show significant alterations (Fig EV1D,E). A similar tendency was observed in

the cerebrocortex of these animals (Fig EV1B), whereas no differences were detected in the cerebellum (Fig EV1C). These results suggest that tunicamycin can exert effects on UPR signaling in the brain differentially with age, particularly impacting the aged hippocampus. Finally, to exclude possible systemic effects of tunicamycin treatment, we injected the ER stressor directly into the hippocampus of young, middle-aged, or aged animals (Fig 1C). We successfully recapitulated the results obtained following intraperitoneal

**Table 1. Significantly altered genes in RNA-seq comparing the hippocampus of demented patients with controls (fold change > 1.2) in the Aging, Dementia and Traumatic injury Study database. Most altered genes compose a functional network of interactions related to unfolded protein binding and processing. Table indicates gene symbols, fold changes, and enriched terms in gene ontology and Kyoto Encyclopedia of Genes and Genomes databases.**

Gene	Fold change	Gene ontology	KEGG
HSPA1A	2.02	Response to unfolded protein	Protein processing in ER
DNAJB1	1.98	Response to unfolded protein	Protein processing in ER
HSPA6	1.76	Response to unfolded protein	Protein processing in ER
HSPA1B	1.74	Response to unfolded protein	
SERPINH1	1.54	Response to unfolded protein	
BAG3	1.3	Protein folding	
HSPB1	1.3	Protein folding, refolding	

injections, observing decreased levels of *Xbp1s* in the hippocampus of middle-aged and aged animals 24 h after exposure when compared with young mice (Fig 1E). As a control, this ER stress-triggering paradigm did not result in differential neurotoxicity during aging as measured by FluoroJade-C staining in the site of injection (Fig EV1F,G).

Increased generation of reactive oxygen and nitrogen species, such as nitric oxide (NO), has been observed during aging (Go & Jones, 2017). Previous reports indicated that S-nitrosylation of IRE1 inhibits its ribonuclease activity (Yang *et al*, 2015), resulting from posttranslational modification of cysteine thiol (or more properly thiolate anion) groups at Cys931 and Cys951 by NO-related species (Nakato *et al*, 2015). Accordingly, we evaluated the levels of S-nitrosylation of IRE1 (abbreviated SNO-IRE1) during normal brain aging. We measured the ratio of SNO-IRE1 to input IRE1 by biotin-switch assay in the brains of young and old animals and found a significant increase in this ratio in aged samples (Fig 1F, Figure Source Data 1–2). This result may potentially account, at least in part, for the decrease in IRE1 activity and thus compromised ability to adapt to ER stress with age. Notably, when we also performed standard immunoblots of IRE1 to quantify levels by densitometry in young and aged animals, we found that total IRE1 decreased with aging (Fig 1G, Figure Source Data 3), as suggested previously based on mRNA levels (Gavilán *et al*, 2006). Thus, while the absolute level of S-nitrosylated IRE1 may not be very different in young versus aged brain, the proportion of SNO-IRE1 significantly increases with age (Fig 1F,G, Figure Source Data 1–3), suggesting overall inhibition of its enzyme activity. These results suggest that the occurrence of specific molecular alterations in the aging hippocampus interfere with the capacity to adapt to ER stress.

#### Genetic disruption of IRE1-XBP1s accelerates or exacerbates aging-associated cognitive decline

To evaluate and quantify cognitive decline associated with normal aging in rodents, we assessed young (3–6 months old), middle-aged (12–14 months old), and aged (18–20 months old) mice using the novel object recognition (NOR), novel object location (NOL), contextual fear conditioning (CFC), and Barnes maze tests; all of which have been previously reported to be sensitive to age-dependent alterations (Shoji *et al*, 2016). Importantly, aged mice interacted with objects in the same amount of time as young animals

(Figs EV1H and 1J), thus excluding age-related motor or sensory alterations that could impact the evaluation of the tests. Moreover, animals at all ages did not exhibit intrinsic preferences for the randomized objects (Fig EV1I) used in the tests nor the quadrants of the arena (Fig EV1K), and their performance was not impacted when evaluated at middle age and again at advanced age (Fig EV1L).

To begin to assess the role of the UPR in brain health span, we conditionally ablated the RNase domain of IRE1 in the nervous system using a CRE transgenic mouse line driven by the Nestin promoter (IRE1<sup>CKO</sup>) for general deletion in nervous tissue (Fig EV2A) at the stage of neural progenitor cells (Duran-Aniotz *et al*, 2017; Appendix Figs S1A and S2 for detailed workflow). Remarkably, middle-aged IRE1<sup>CKO</sup> animals lost their capacity to discriminate between novel objects in the NOR test when compared with Cre-negative/wild-type (WT) littermates (IRE1<sup>WT</sup>). Note that control animals only displayed poor performance at advanced age (Fig 2A). The NOL test highlighted the impaired capacity of middle-aged or older WT animals to discriminate newly located objects (Fig EV2B). Importantly, aged IRE1<sup>CKO</sup> animals also showed this deficit, while younger IRE1<sup>CKO</sup> mice exhibited normal behavior (Fig EV2B). The apparent absence of phenotypes in IRE1<sup>CKO</sup> during youth on these two tests suggests the occurrence of age-dependent deficits after IRE1 ablation. To further examine this hypothesis, we evaluated an additional cohort of mutant mice with a deletion of IRE1 mediated by Cre driven by the Camk2a promoter (IRE1<sup>CKO/Cak</sup>; Appendix Fig S1B). Notably, we could recapitulate the same findings observed in IRE1<sup>CKO</sup> mice in the NOR test, with young animals exhibiting no alterations upon IRE1 ablation but middle-aged IRE1<sup>CKO/Cak</sup> displaying impaired capacity to discriminate novel objects when compared with age-matched controls (Fig EV2C).

IRE1 signaling has various outputs in addition to controlling XBP1 mRNA splicing, including degradation of mRNAs and regulation of cell signaling (Hetz *et al*, 2020). Accordingly, to further validate our results, we generated a small cohort of XBP1 conditional knockout animals (XBP1<sup>CKO</sup>; Appendix Fig S1C). This model manifests normal IRE1 expression but lacks XBP1 in the hippocampus. Using this additional mouse model, we recapitulated the deficits observed in middle-aged IRE1<sup>CKO</sup> and IRE1<sup>CKO/Cak</sup> mice on the NOR test (Fig EV2D). Since XBP1 ablation has been reported in some cases to trigger aberrant phenotypes because of compensatory IRE1 overactivation (Lee *et al*, 2008, 2011; Hur *et al*, 2012), we focused



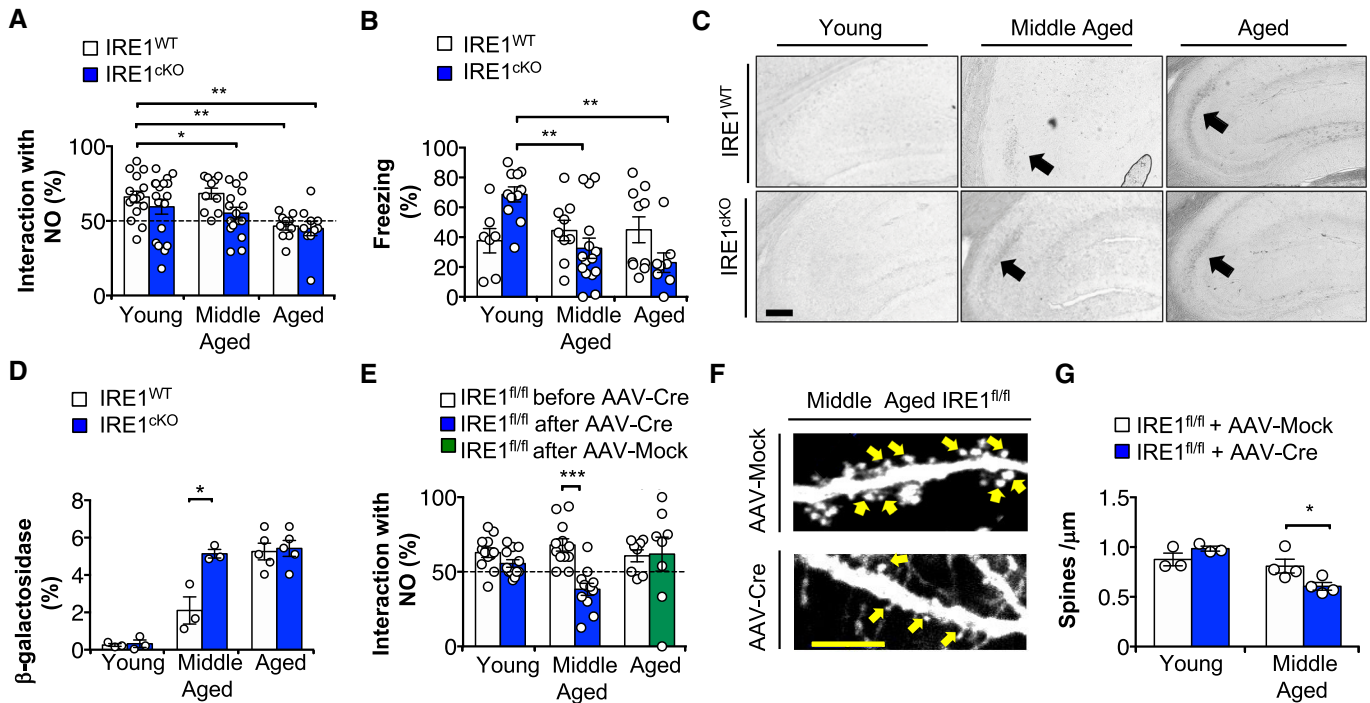


**Figure 2. Genetic ablation of the IRE1 pathway in the brain accelerates and exacerbates age-associated cognitive decline in mammals.**

A–D Young (3–6 months), middle-aged (12–14 months) and aged (18–20 months) conditional knockout for IRE1 (IRE1<sup>ckKO</sup>) and their littermates flox/flox control animals (IRE1<sup>WT</sup>) were evaluated in new object recognition test (A), and contextual fear conditioning test (B); (please refer to Appendix Figures for complete workflow). (A) Mean and s.e.m. of the difference in exploration time between novel and familiar objects divided by the total amount of exploration time of both objects (%).  $n = 15, 18; 10, 16; 10, 10$ . Two-way ANOVA followed by Holm–Sidak’s multiple comparison test;  $P$ -values: Age = 0.0001; Genotype = 0.02; Interaction = 0.40. (B) Mean and s.e.m. of percentage of time of freezing in the first minute before sound presentation in test day (day 2).  $N = 7, 11; 9, 15; 10, 8$ . Two-way ANOVA followed by Holm–Sidak’s multiple comparison test;  $P$ -values: Age = 0.0341; Genotype = 0.87; Interaction = 0.0018. (C) Representative photomicrographs of  $\beta$ -galactosidase staining of hippocampal slices derived from young (3 months), middle-aged (12 months) and aged (22–24 months) of IRE1<sup>WT</sup> or IRE1<sup>ckKO</sup> animals. Magnification: 20 $\times$ ; scale bar: 200  $\mu$ m. Arrows indicate  $\beta$ -galactosidase staining. (D) Mean and SEM of percentage of  $\beta$ -galactosidase staining in CA3 region ( $n = 3$ –5 animals/group).  $P$  computed by unpaired Student’s  $t$ -test within each age-matched group.

E Young (3 months) and middle-aged (12 months) IRE1 flox/flox (IRE1<sup>fl/fl</sup>) mice were evaluated in the new object recognition test before and after intrahippocampal injections with AAV2-Cre. Controls were injected with AAV2-Mock. Graph indicates mean and SEM of the difference in exploration time between novel and familiar objects divided by the total amount of exploration time of both objects (%) before and after treatment.  $n = 12, 12, 8$ . Two-way ANOVA with repeated measurements followed by Holm–Sidak’s multiple comparison test;  $P$ -values: AAV-Cre treatment: 0.0001; Age = 0.08; Interaction = 0.0053.

F Representative confocal images of dendritic spines (arrows) in the CA1 region of middle-aged IRE1<sup>WT</sup> animals injected with AAV-Mock or AAV-Cre. 60 $\times$  magnification, scale bar: 5  $\mu$ m.

G Mean and SEM of spine density per  $\mu$ m ( $n = 3, 3; 4, 4$  animals).  $P$  computed by unpaired Student’s  $t$ -test within each age-matched group.

Data information: All graphs indicate  $P$ -values with the following legend: \* $P < 0.05$ ; \*\* $P < 0.01$ ; \*\*\* $P < 0.005$ .

our analysis on IRE1-deficient animals. In addition, we have previously reported that young XBP1<sup>ckKO</sup> animals displayed diminished performance on fear conditioning and maze-based tests (Martínez et al, 2016), thus obfuscating interpretation of results when age-dependent cognitive decline is being assessed. Hence, we evaluated a cohort of IRE1<sup>ckKO</sup> animals and their control littermates at different ages using the CFC test that evaluates freezing responses before and after presentation of a tone. On the day of testing, our analysis showed that young IRE1<sup>ckKO</sup> mice displayed increased freezing before presentation of the tone, indicative of altered contextual fear memory acquisition. With aging, however, freezing on this test significantly decreased (Fig 2B). Importantly, these results were not observed in WT littermates, which presented similar responses throughout aging (Fig 2B). Collectively, assessment of NOR and CFC data throughout aging suggested that genetic ablation of IRE1

in the nervous system may accelerate the emergence of age-associated alterations in cognitive function.

### IRE1<sup>ckKO</sup> displays early appearance of senescent cells in the hippocampus

Previous findings suggested that an increased number of senescent cells in brain tissue correlates with age-dependent cognitive decline (Baker & Petersen, 2018). To determine whether disruption in the IRE1 pathway in the brain resulted in altered senescence, we evaluated the number of senescent cells using  $\beta$ -galactosidase and p- $\gamma$ -H2AX staining in hippocampal tissue. Histological analysis indicated progressive accumulation of senescent cells in the hippocampus as animals aged (Figs 2C,D and EV2E–G). Notably, an increase in the number of senescent cells comparable with that

found in aged controls was observed in the brains of middle-aged IRE1<sup>CKO</sup> animals (Figs 2C,D and EV2E–G). These results suggest that genetic disruption of the IRE1 pathway in the hippocampus accelerates the appearance of senescent cells in the hippocampus, and this finding correlates with the development of cognitive impairment.

### IRE1 deletion in the adult hippocampus accelerates age-dependent cognitive decline

Genetic manipulations during development could result in compensatory mechanisms that do not necessarily reflect the direct contribution of a gene to the observed phenotype in the adult animal. To determine whether ablation of IRE1 expression in the adult could alter the cognitive capacity of mice in an age-dependent manner, we locally delivered adeno-associated viral vectors (AAV) to express CRE recombinase or control vector expressing GFP (AAV-Mock) into the hippocampus of IRE1 floxed animals (Appendix Fig S1D). This strategy significantly reduced the levels of IRE1 mRNA in the hippocampus (Fig EV2H,I) and allowed us to test animals before and after AAV injections for comparison. Middle-aged or young mice were tested on the NOR assay before AAV-CRE injection and then monitored again 4 weeks after brain surgery. Remarkably, targeting IRE1 in the hippocampus of middle-aged mice impaired the capacity to discriminate novel objects when compared with the group that received empty vector (Fig 2E). Importantly, this experimental setup did not impact the performance of young animals (Fig 2E), and thus recapitulated our previous findings in IRE1<sup>CKO</sup> animals regarding the occurrence of an age-dependent effect of IRE1 ablation that accelerated cognitive decline.

Previous reports indicated that normal aging results in a decrease in the number of dendritic spines, correlating with impaired cognition (Dickstein *et al.*, 2013). To determine possible morphological alterations triggered by IRE1 deficiency during aging, we evaluated dendritic spine density on pyramidal neurons in the CA1 region following AAV-GFP delivery to label neuronal morphology and dendritic arbors. Morphological assessment using confocal microscopy indicated that middle-aged IRE1<sup>fllox/fllox</sup> mice displayed a decrease in the density of dendritic spines in the CA1 region following AAV-Cre/GFP injection when compared with age-matched littermates injected with control vector expressing only GFP (Fig 2F,G). Importantly, as a control, expression of Cre in the brain of young IRE1<sup>fllox/fllox</sup> animals did not alter the distribution of dendritic spines (Fig 2F,G), confirming the occurrence of age-related alterations. Taken together, our results indicate that targeting IRE1 expression in the adult brain results in age-dependent cognitive decline and morphological alterations, supporting our previous observations on IRE1<sup>CKO</sup>, IRE1<sup>CKO/Cak</sup>, and XBP1<sup>CKO</sup> mice.

### Aged Tg<sup>XBP1s</sup> animals are less susceptible to age-dependent cognitive decline and display reduced senescent cells in the hippocampus

To test the consequences of artificially bolstering an adaptive UPR during aging, we developed strategies to increase the levels of the spliced and active form of XBP1 in the brain (Fig EV3A). For this purpose, we initially evaluated cognitive performance during aging

of transgenic mice that overexpressed XBP1s under the control of the PrP promoter (Martínez *et al.*, 2016; referred to here as Tg<sup>XBP1s</sup>, Appendix Figs S1E and S3, for detailed workflow).

Notably, XBP1s overexpression prevented the appearance of age-related deterioration in brain function with middle-aged or advanced-age mice retaining their ability to discriminate between newly located objects and novel objects compared with WT littermates (Fig 3A,B). We have previously shown that young Tg<sup>XBP1s</sup> perform better than young controls in a memory flexibility paradigm based on spatial testing (Martínez *et al.*, 2016), indicating that Tg<sup>XBP1s</sup> mice exhibit increased learning capacity in both spatial memory acquisition and flexibility. Here, we aimed to evaluate whether this transgenic line can maintain such capacity throughout aging using the Barnes Maze test, focusing mainly on spatial memory acquisition. Importantly, young Tg<sup>XBP1s</sup> performed similarly to young Non-Tg littermates, as indicated by the latency to find the target during 4 days of training (Fig EV3B). Remarkably, middle-aged and aged Tg<sup>XBP1s</sup> mice performed better than age-matched control littermates, displaying decreased latency to find the target hole during both the skill acquisition days and on the test day (Fig 3C,D). Finally, using the CFC test, we were not able to detect spontaneous age-related phenotypes in WT animals, and we also could not detect significant alterations in freezing responses between Tg<sup>XBP1s</sup> and age-matched littermates before tone presentation (Fig EV3C).

Next, we measured the content of senescent cells in the hippocampus of Tg<sup>XBP1s</sup> animals during aging. Remarkably, histological analysis of aged animals indicated a significant decrease in the number of senescent cells in aged Tg<sup>XBP1s</sup> compared with age-matched WT littermates (Fig 3E,F). Collectively, our behavioral and morphological assessments indicate that forced expression of XBP1s in the brain over the life span of an animal prevents age-associated cognitive decline.

### XBP1s overexpression in Tg<sup>XBP1s</sup> animals impacts age-related changes in the hippocampal proteome, affecting proteins involved in neuronal function and neurodegenerative diseases

To further evaluate the effects of XBP1s overexpression on aging at the protein level, we performed an unbiased proteomic analysis of hippocampal tissue derived from animals at different ages during XBP1s overexpression (Fig 4A). We observed a strong positive correlation between the proteomic changes in middle-aged and aged mice compared with young mice ( $r = 0.53$ ) (Fig 4B). Notably, these age-related alterations were largely restored by XBP1s overexpression in middle-aged ( $r = -0.49$ ) and aged mice ( $r = -0.46$ ), with nearly 70% of the proteins reversing their pattern of change (Fig 4B). By contrast, changes induced in the proteome by XBP1s overexpression in early life were unrelated to the changes observed during aging (Fig 4B). Next, we identified the proteins downregulated during mouse aging and upregulated upon XBP1s overexpression, or vice versa, in middle-aged and aged mice (Fig EV4A). The overlap between proteins regulated in opposite directions was statistically significant in all these analyses (Fig EV4A).

To investigate possible molecular pathways that may explain the protective effects of XBP1s overexpression during normal brain aging in mice, we performed a gene set enrichment analysis (GSEA),

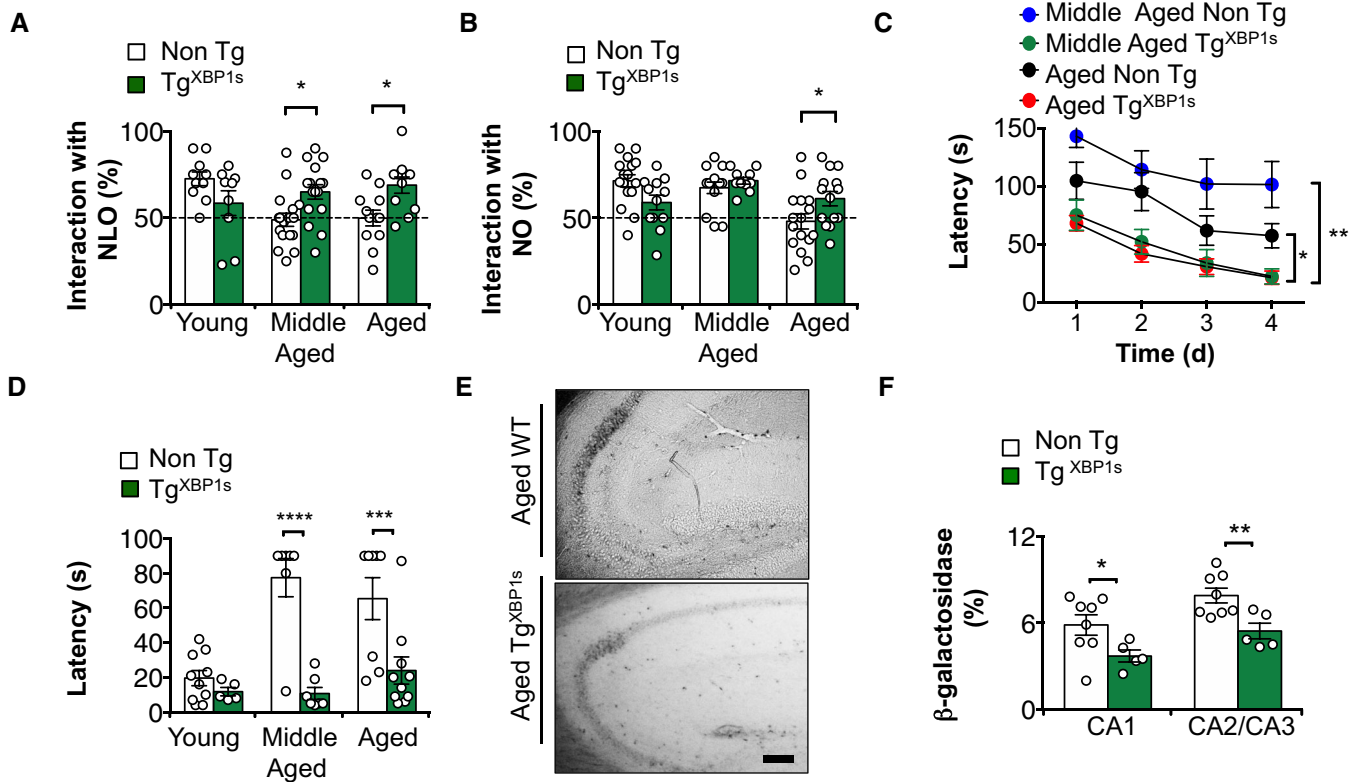


**Figure 3. Enforced expression of XBP1s in the brain prevents age-associated cognitive decline in mammals.**

A–D Young (3–6 months), middle-aged (12–14 months) and aged (18–20 months) Tg<sup>XBP1s</sup> and their littermate control animals Non-Tg were evaluated in new object location (A), new object recognition (B), Barnes maze (C, D). Please refer to Appendix Figs S1E and S3 for complete workflow. (A) Mean and s.e.m. of the difference in exploration time between displaced and familiar objects divided by the total amount of exploration time of both objects (%).  $n = 10, 9; 17, 16; 12, 11$ ; Two-way ANOVA followed by Holm–Sidak’s multiple comparison test;  $P$  (Interaction between Age and Genotype) = 0.0048. (B) Mean and s.e.m. of the difference in exploration time between novel and familiar objects divided by the total amount of exploration time of both objects (%).  $n = 16, 12; 14, 10; 16, 14$ ; Two-way ANOVA followed by Holm–Sidak’s multiple comparison test;  $P$  (Interaction between Age and Genotype) = 0.0186. (C) Mean and SEM of latencies to find the target hole in the Barnes maze test during 4 days of training comparing middle-aged (12 months) and aged (20–22 months) Tg<sup>XBP1s</sup> with littermate controls.  $n = 10, 5; 7, 7; 8, 10$ ; Two-way ANOVA with repeated measurements followed by Holm–Sidak’s multiple comparison test;  $P$  (Genotype) = 0.0004. (D) Mean and SEM of latencies to find the target hole in test day.  $n = 10, 5; 7, 7; 8, 10$ ; Two-way ANOVA followed by Holm–Sidak’s multiple comparison test;  $P$ -values: Age = 0.0013; Genotype < 0.0001; Interaction = 0.0042.

E Representative images of β-galactosidase staining of hippocampal slices derived from aged (22–24 months) Tg<sup>XBP1s</sup> and WT animals. Magnification: 20×; scale bar: 200 μm.

F Mean and SEM of percentage of area stained by β-galactosidase in the hippocampus of aged (20–24 months) Tg<sup>XBP1s</sup> compared to littermate controls.  $n = 8, 5$ ; unpaired Student’s  $t$ -test.

Data information: All graphs indicate  $P$ -values with the following legend: \* $P < 0.05$ ; \*\* $P < 0.01$ ; \*\*\* $P < 0.005$ ; \*\*\*\* $P < 0.001$ .

comparing significant proteomic alterations between young and aged WT animals (Fig 4A). This analysis revealed clusters of proteins involved in long-term potentiation, calcium signaling, and metabolic control (Fig EV4B; Table 2; please refer to Dataset EV2 for detailed analysis). The comparison between middle-aged with aged WT animals revealed additional clusters of proteins related to synaptic vesicle recycling, endocytosis, and cytoskeletal dynamics, among other processes (Fig EV4B; Table 2).

Next, we compared Tg<sup>XBP1s</sup> animals with age-matched littermates (Fig 4A) and found similar enriched pathways related to aging in WT animals (Figs 4C and EV4C,D; Table 3; Dataset EV2 for detailed analysis). This analysis highlighted proteins involved in neurotransmission (long-term potentiation, neurofilaments, glutamatergic synapses, exocytosis, and myelin sheath), potentially underlying the

functional improvements observed in these animals at the cognitive level. Interestingly, enriched terms were also associated with several age-related neurodegenerative diseases (amyotrophic lateral sclerosis [ALS], prion diseases, and AD; Figs 4C and EV4C,D, Table 3).

To evaluate the potential relevance of the effect of XBP1s overexpression in humans, we identified the top-ranking proteins that were downregulated during mouse aging and upregulated upon XBP1s overexpression, or vice versa, in middle-aged and aged mice (Fig 4D, left), and then determined whether the expression of these proteins changed with age in the human hippocampus (Fig 4D, right). In aged mice, proteins downregulated during aging and upregulated by XBP1s overexpression (Fig 4D, dark green/blue dots) tended to be negatively correlated with human aging (manifesting decreased expression with age). Additionally, proteins upregulated



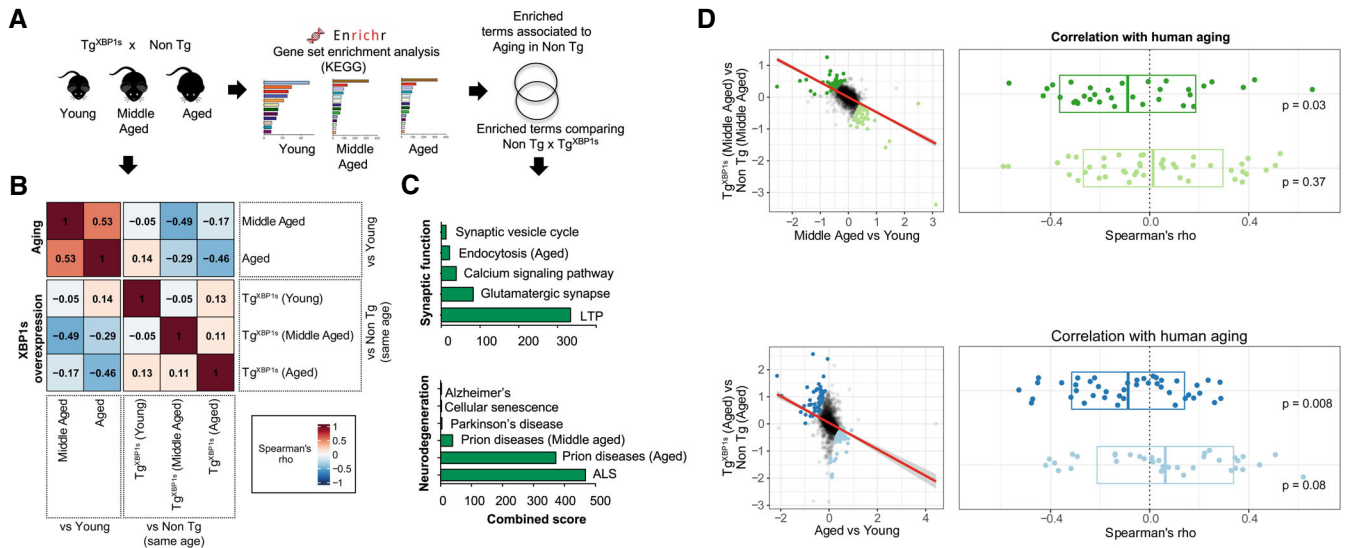


**Figure 4. XBP1s overexpression in the nervous system prevents proteomic alterations observed during brain aging.**

**A** Scheme depicting the rationale in proteomic analysis for Tg<sup>XBP1s</sup> animals. Proteomic alterations in the hippocampus of Tg<sup>XBP1s</sup> mice were compared to age-matched Non-Tg littermates followed by gene set enrichment analysis using KEGG libraries through EnrichR platform. Enriched terms were compared to the ones found during aging in Non-Tg mice.

**B** Correlation matrix comparing the proteomic changes observed during normal aging and those induced by XBP1s overexpression. Colors indicate Spearman's rank correlation coefficient.

**C** Graphs depict most enriched terms based on combined scores computed by EnrichR comparing middle-aged and aged Tg<sup>XBP1s</sup> with age-matched controls. Terms were divided into two graphs related to synaptic function or neurodegeneration. LTP: long-term potentiation; ALS: amyotrophic lateral sclerosis.

**D** In middle-aged and aged mice, top 50 proteins leading to the reversal of the aging-related changes by XBP1s (colored dots in scatter plots) were selected based on the effect sizes in both comparisons (left). We analyzed the correlation of these proteins with age in a temporal transcriptomic study of the human hippocampus<sup>75</sup> (jitter plots, right). Cross bar in the jitter plot indicates the mean ± 1SD of each sample (n = 3–4 samples/group). P-values at the right side of the plot were calculated using a t-test to evaluate if the average was less or greater than zero (n = 3–4 samples/group).

during aging and downregulated by XBP1s (Fig 4D, light green/blue dots) showed a trend of positive correlation in the aged human brain. Those findings did not reach statistical significance in two other human datasets analyzed (Fig EV4E). Overall, our analysis indicated that overexpression of XBP1s in the aging brain reversed changes in expression of a cluster of proteins that partially superimposed with previously observed protein alterations in the human brain with aging.

**XBP1s gene delivery by AAV into the hippocampus of aged animals reverses age-associated cognitive decline**

To assess whether aberrant proteostasis and its impact on brain function during aging can be restored, we used a gene transfer approach to deliver XBP1s into the hippocampus. For this purpose, we performed bilateral injections of AAV expressing XBP1s into the hippocampus of aged mice that already manifested cognitive decline (Figs 5A and EV5A). Remarkably, the administration of AAV-XBP1s to middle-aged and aged animal brains improved performance in various cognitive tests compared with age-matched animals injected with control virus (please refer to Appendix Figs S1F and S4 for detailed workflow). Middle-aged and aged animals injected with AAV-XBP1s manifested the ability to discriminate novel objects or newly located objects (Fig 5B,C). Additionally, evaluation in the Barnes maze indicated that aged mice receiving AAV-XBP1s

displayed a significant decrease in latency to find the target on the second day of memory acquisition (Fig 5D), although no significant differences were found on the test day (Fig EV5B). Moreover, analysis of the CFC indicated that aged mice injected with AAV-XBP1s into the hippocampus showed an increased freezing response following tone presentation compared to age-matched controls, although no significant alterations were found before tone presentation (Fig 5E). This result suggests that aged animals treated with AAV-XBP1s have improved fear conditioning memory, although contextual memory was not impacted. Taken together, our behavioral analyses indicated that XBP1s overexpression in the hippocampus was sufficient to reverse several aging-associated cognitive alterations.

Next, to confirm that the age-associated phenotypes observed in IRE1-deficient animals were dependent on XBP1 expression, we treated middle-aged IRE1<sup>CKO</sup> mice with AAV-XBP1s. We performed the NOR test before and after bilateral intrahippocampal injections of AAV-XBP1s or control viral constructs (Appendix Figs S1G and S5). As expected from our results reported in Fig 2A, the middle-aged IRE1<sup>CKO</sup> were unable to differentiate novel objects (Fig 5F). Notably, however, treatment with AAV-XBP1s, but not control AAV, restored their ability to discriminate between novel objects within 4 weeks of the injection (Fig 5F). These results strongly support the notion that XBP1s is a major effector of IRE1-dependent preservation of cognitive function during aging.

**Table 2. Most enriched terms in KEGG database comparing mice in different ages. Table indicates terms, associated genes and combined score computed in EnrichR platform.**

Enriched term	Genes	Score
<b>Young vs Aged</b>		
Long-term potentiation	PPP3R1;ADCY1;CALM2	321.4
Glycolysis/ Gluconeogenesis	ENO1;ENO2	130.4
RNA degradation	ENO1;ENO2	97.5
Insulin secretion	ADCY1;STX1A	92.9
Calcium signaling pathway	PPP3R1;ADCY1;CALM2	76.8
Glucagon signaling pathway	PPP3R1;CALM2	73.3
HIF-1 signaling pathway	ENO1;ENO2	71.3
Prion diseases	C1QA	71
Glutamatergic synapse	PPP3R1;ADCY1	62.73
Amyotrophic lateral sclerosis	PPP3R1	40.3
Alzheimer disease	PPP3R1;CALM2	33.7
Cellular senescence	PPP3R1;CALM2	31
cAMP signaling pathway	ADCY1;CALM2	25.4
Synaptic vesicle cycle	STX1A	23.4
GABAergic synapse	ADCY1	18.8
Longevity regulating pathway	ADCY1	15.7
Neurotrophin signaling	CALM2	12.2
Dopaminergic synapse	CALM2	10.3
<b>Middle-aged vs Aged</b>		
ECM-receptor interaction	COL1A1;COL1A2;HSPG2	48.8
Necroptosis	H2AFY1;H2AFY2;H2AFX;H2AFV	29.61
Glycolysis	ENO1;ENO2	26.2
Endocytosis	DNM3;ARPC3;WIPF3; NEDD4L;ARPC5	25.1
Synaptic vesicle cycle	DNM3;STX1A	21.21
SNARE interactions	STX1A	15.82
Prion diseases	NCAM2	15.14
Alzheimer disease	COX5A;CALM2;UQCRH	14.6
HIF-1 signaling pathway	ENO1;ENO2	13.13
Oxidative phosphorylation	COX5A;UQCRH	8.57
Insulin signaling pathway	PRKAR2B;CALM2	8.04
Parkinson disease	COX5A;UQCRH	7.56
Ribosome	RPL23;RPLP2	5.62
Long-term potentiation	CALM2	5.39
Calcium signaling pathway	ATP2B4;CALM2	4.61
Huntington disease	COX5A;UQCRH	4.48
cAMP signaling pathway	ATP2B4;CALM2	3.74

### **XBPs gene delivery by AAV into the hippocampus of aged mice improves electrophysiological and morphological parameters**

Age-associated cognitive impairment involves alterations in the circuitry of the hippocampus, affecting its electrical activity (Dickstein *et al*, 2013). Therefore, we evaluated electrophysiological

**Table 3. Most enriched terms in KEGG database comparing Tg<sup>XBPs</sup> with age-matched WT mice. Table indicates enriched terms and their associated genes. Symbols highlight when those terms are enriched in Tg<sup>XBPs</sup> animals within each age-comparison.**

Enriched terms	Genes
<b>Synaptic function</b>	
Synaptic vesicle cycle <sup>a</sup>	CLTB;CLTA;SLC6A11;SLC17A7; SLC1A3
Long-term potentiation <sup>a</sup>	GRIA1;PPP3CA;GRIN2A;RAP1B;CAMK2D; PPP3R1;ADCY1
Glutamatergic synapse <sup>a</sup>	GRIA1;PPP3CA;GRIN2A;SLC17A7;PPP3R1; SLC1A3;ADCY1
Calcium signaling pathway <sup>b</sup>	PPP3CA;GRIN2A;PTK2B;SLC8A1;CAMK2D; PPP3R1;ADCY1; ATP2B4
Dopaminergic synapse <sup>a</sup>	GRIA1;PPP3CA;GRIN2A; CAMK2D
Endocytosis <sup>b</sup>	ARPC1A;CLTB;CLTA;ARPC4;WIPF3;HSPA1A; WIPF3;HSPA1A
Long-term depression <sup>c</sup>	GRIA1
cAMP signaling pathway <sup>b</sup>	GRIA1;GRIN2A;RAP1B;CAMK2D;ADCY1; ATP2B4
GABAergic synapse <sup>a</sup>	SLC6A11;ADCY1
Neuroactive ligand-receptor <sup>b</sup>	GRIA1;GRIN2A
MAPK pathway <sup>b</sup>	PPP3CA;CACNG8;TAOK3;STMN1;RAP1B; PPP3R1; TAOK3; HSPA1A
Axon guidance <sup>b</sup>	PPP3CA;CAMK2D;PPP3R1;PTPN11
<b>Neurodegeneration</b>	
ALS <sup>a</sup>	GRIA1;PPP3CA;GRIN2A;PPP3R1;NEFL; NEFM;NEFH
Prion diseases <sup>b</sup>	C1QB;C1QA;NCAM2;HSPA1A
Alzheimer disease <sup>a</sup>	PPP3CA;GRIN2A;PPP3R1
Apoptosis <sup>d</sup>	LMNA;LMNB2;LMNA;LMNB2
Necroptosis <sup>b</sup>	HIST3H2A;H2AFY1;CAMK2D;HIST3H2A;H2AFX
Cellular senescence <sup>a</sup>	PPP3CA;PPP3R1
<b>Metabolism/Bioenergetics</b>	
Glucagon signaling pathway <sup>a</sup>	PPP3CA;LDHB;CAMK2D;PPP3R1
Glycolysis/Gluconeogenesis <sup>c</sup>	LDHB
GnRH signaling pathway <sup>a</sup>	PTK2B;CAMK2D;ADCY1
<b>Other terms</b>	
Spliceosome <sup>d</sup>	HNRNPM;DDX5;HNRNPA3;HNRNPK;SRSF1; SRSF2;HNRNPU;SRSF4;HNRNPC;PRPF19; HSPA1A
Ribosome <sup>a</sup>	RPLP2;RPS13;RPL18

<sup>a</sup>Term enriched in Young and Middle-aged Tg<sup>XBPs</sup>.

<sup>b</sup>Term enriched in Young, Middle-aged and Aged Tg<sup>XBPs</sup>.

<sup>c</sup>Term enriched only Young Tg<sup>XBPs</sup>.

<sup>d</sup>Term enriched in Young and Aged Tg<sup>XBPs</sup>.

parameters of hippocampal slices derived from aged animals injected with AAV-XBPs. Firing rates of CA1 neurons of aged animals (22–24 months old) injected with AAV-Mock or AAV-XBPs were recorded during spontaneous activity or following picrotoxin (PTX) treatment to antagonize GABAergic inhibitory interneurons in order to foster excitatory activity in the hippocampal circuit. We observed a decrease in basal firing rates (Fig 6A) and bursting

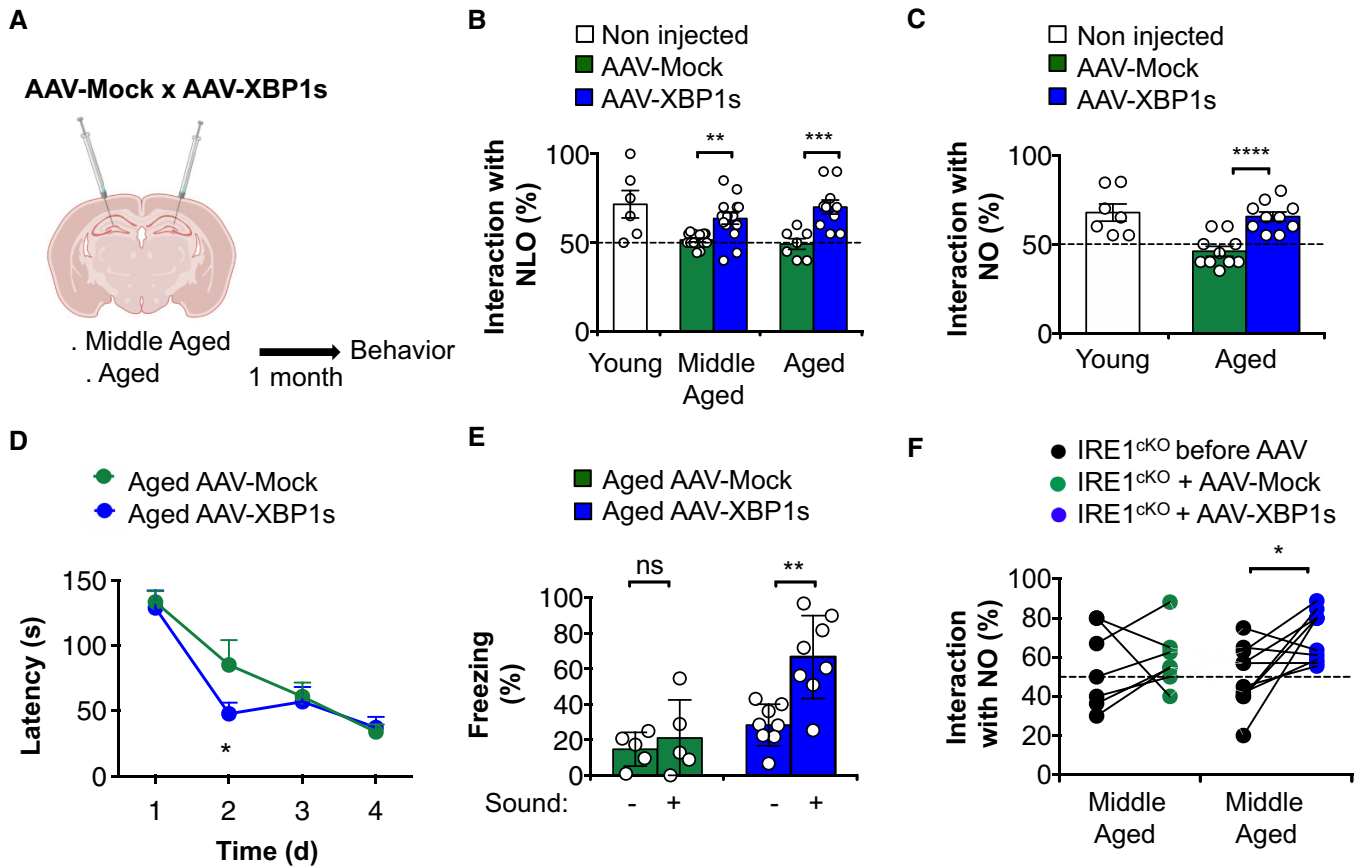


**Figure 5. XBP1s gene delivery to aged animals reverses age-associated behavioral deficits.**

- A Middle-aged (12 months) and aged (18 months) WT mice were injected in both hippocampus with AAV-XBP1s or AAV-Mock. Following 1 month of injection, they were evaluated in the new object location, new object recognition, Barnes Maze and contextual fear conditioning tests (please refer to Appendix Figures for complete workflow).
- B Mean and s.e.m. of the difference in exploration time between displaced and familiar objects divided by the total amount of exploration time of both objects (%). ( $n = 6; 13, 14; 7, 10$ ). Young animals' performance was plotted, for comparison. Two-way ANOVA followed by Holm-Sidak's multiple comparison test;  $P$  (AAV Treatment)  $< 0.0001$ .
- C Graph indicates mean and s.e.m. of the difference in exploration time between novel and familiar objects divided by the total amount of exploration time of both objects (%).  $n = 7, 10, 10$ ; unpaired Student's  $t$ -test. Young animals' performance was plotted for comparison.
- D Mean and s.e.m. of latencies to find target for each group during 4 days of testing ( $n = 5, 8$ ; Multiple Student's  $t$ -test within each day).
- E Mean and s.e.m. of freezing response (%) in the retention day of the CFC test before and after sound presentation ( $n = 5, 8$ ; Two-way ANOVA followed by Holm-Sidak's multiple comparison test;  $P$ -values: Sound = 0.0027; AAV treatment = 0.0002; Interaction = 0.021).
- F Middle-aged (12 months) IRE1<sup>cKO</sup> were evaluated in the NOR test before and after AAV-XBP1s intrahippocampal injections. Controls were injected with AAV-Mock. Graph indicates mean and s.e.m. of the difference in exploration time between novel and familiar objects divided by the total amount of exploration time of both objects (%) before and after treatment.  $n = 7, 10$ ; two-way ANOVA with repeated measurements followed by Holm-Sidak's multiple comparison test;  $P$  (AAV Treatment): 0.0436.

Data information: Graphs indicate  $P$ -values with the following legend: \* $P < 0.05$ ; \*\* $P < 0.01$ ; \*\*\* $P < 0.005$ ; \*\*\*\* $P < 0.001$ .

activity (Fig 6B) in hippocampal CA1 neurons after treating aged animals with AAV-XBP1s. Additionally, increased firing rates and bursting activity were observed in CA1 neurons following PTX treatment in XBP1s-overexpressing animals (Fig 6A,B). Importantly, induction of long-term potentiation (LTP), thought to represent an electrical correlate of learning and memory, was significantly improved in hippocampal slices derived from aged mice treated with AAV-XBP1s compared with controls (Fig 6C; see fiber volley amplitudes in Fig EV5C). Correlating with these findings, we observed a significant increase in dendritic spine density in CA1 neurons compared with age-matched control animals (Fig 6D). Finally, we measured the distribution of senescent cells in the hippocampus and

found decreased accumulation of  $\beta$ -galactosidase activity (Fig 6E) and  $p$ - $\gamma$ -H2AX immunolabeling (Fig 6F) in the hippocampus following XBP1s overexpression. Taken together, these results suggest that XBP1 expression in the aged hippocampus improves behavioral, morphological, and electrophysiological parameters associated with normal brain aging.

#### XBP1s gene delivery modifies pathways related to synaptic function and neurodegenerative disease

Finally, we evaluated proteomic changes in the hippocampus of aged animals treated with AAV-XBP1s. GSEA indicated that the

administration of AAV-XBP1s into the brain modified the expression of proteins involved in synaptic function, neurofilaments, and vesicle cycle dynamics, in addition to proteins associated with neurodegenerative diseases (Figs 6G,H and EV5D, Table 4; please refer to Dataset EV2, for full analysis). These findings are similar to those we obtained in Tg<sup>XBP1s</sup> animals. We also detected important changes in proteins related to the extracellular matrix (Table 4), including collagens, laminin subunits, and heparan sulfate proteoglycan 2. Other changes included glycolysis/gluconeogenesis-related proteins, suggesting an impact on metabolic pathways. Overall, our proteomic profiling suggests that forced expression of XBP1s influences age-associated protein alterations related to synaptic function and

are consistent with the positive effect of XBP1s administration in prolonging brain health span in terms of cognitive function.

## Discussion

In the current study, we provide evidence supporting a protective function of the IRE1-XBP1s axis during aging in sustaining mammalian brain healthspan. These results are based on improved maintenance of synaptic function and enhanced cognitive capacity in the face of aging by manipulating the IRE1-XBP1s pathway. We combined the use of multiple gain- and loss-of-function approaches to

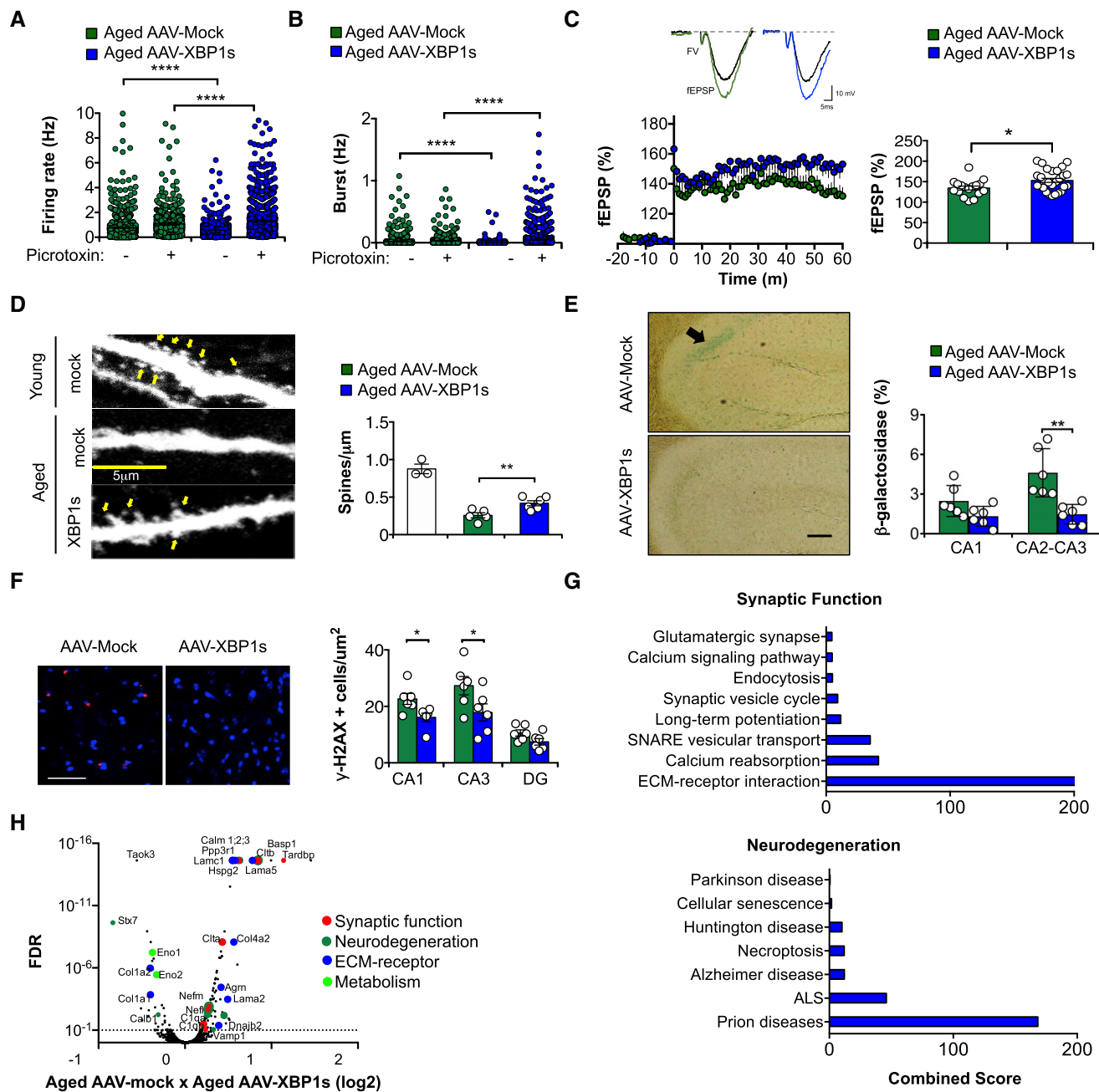


Figure 6.

**Figure 6. XBP1s gene delivery to aged hippocampus reverses age-associated phenotypes at the morphological and electrophysiological levels.**

- A Basal (–) and picrotoxin-induced (+) of firing rates (Mean and s.e.m.) were measured in hippocampal brain slices from aged mice (24 months) injected with AAV2-Mock or AAV2-XBP1s ( $n = 633$ – $832$  neurons;  $n = 6, 9$  animals, respectively; Kolmogorov–Smirnov test).
- B Basal (–) and picrotoxin-induced (+) burst activity (Mean and s.e.m.) were measured in Hippocampal brain slices from aged mice injected with AAV2-Mock or AAV2-XBP1s ( $n = 832, 644$  neurons from 3–4 animals, Kolmogorov–Smirnov test).
- C Left panel: Mean and s.e.m. of field excitatory postsynaptic potentials amplitudes in brain slices derived from aged animals injected with AAV2-Mock or AAV2-XBP1s (24 months). Recordings of PEPs following 1 h after theta burst stimulus (TBS) to induce LTP. Right panel: Mean and s.e.m. of PEPs in the last 10 min following TBS.  $n = 6, 9$  animals, respectively;  $n = 17$ – $28$  slices/animal, unpaired Student's *t*-test).
- D Left panel: Representative images showing dendritic spines of aged (22–24 months) animals injected with AAV2-eGFP (mock) or with AAV2-XBP1s (arrows indicate dendritic spines). Young animal dendrite is shown for reference.  $60\times$  magnification. Scale bar:  $5\ \mu\text{m}$ . Right panel: Mean and s.e.m. of spine density per  $\mu\text{m}$  for indicated experimental groups ( $n = 24, 53$  and  $35$  dendrites from 3, 5 and 6 animals, respectively; unpaired Student's *t*-test).
- E Left panel: Representative images of  $\beta$ -galactosidase staining of hippocampal slices derived from aged mice injected with AAV2-Mock or AAV2-XBP1s (arrow indicate  $\beta$ -galactosidase staining). Magnification  $20\times$ ; scale bar,  $200\ \mu\text{m}$ . Right panel: Histograms show mean and s.e.m. of percentage of  $\beta$ -galactosidase-stained area.  $n = 6, 6$ ; unpaired Student's *t*-test.
- F Left panel: Immunofluorescence of  $p$ - $\gamma\text{H2aX}$  (red) counterstained with nuclei (blue) comparing aged mice injected with AAV-Mock or AAV-XBP1s. Magnification:  $40\times$ ; Scale bar:  $50\ \mu\text{m}$ . Right panel: Histograms show mean and s.e.m. of percentage of  $p\gamma\text{H2A}$ - positive cells; unpaired Student's *t*-test comparing the aged groups ( $n = 6, 6$  animals/group; unpaired Student's *t*-test).
- G Following LC-MS/MS analysis of the hippocampal proteome, gene set enrichment analysis was performed using EnrichR with Kyoto Encyclopedia of Genes and Genomes (KEGG) database. Graphs depict most enriched terms based on combined scored computed by EnrichR platform comparing aged mice injected with AAV-Mock or AAV-XBP1s. Terms were divided in two graphs related to synaptic function or neurodegeneration.
- H Volcano plot for proteomic comparison of hippocampal tissue derived from aged animals injected with AAV-Mock or AAV-XBP1s. FDR (*y*-axis) and fold-change ( $\log_2$ ) (*x*-axis) are indicated. Dotted lines delineate cutoff used to filter genes for functional enrichment analysis. Indicated genes associated with each enriched terms connected to synaptic function, neurodegeneration, metabolism and ECM-receptor interaction are colored.
- Data information: Graphs indicate *P*-values with the following legend: \**P* < 0.05; \*\**P* < 0.01; \*\*\**P* < 0.005; \*\*\*\**P* < 0.001.

target this canonical signaling branch of the UPR to assess its significance in brain function during aging at the cognitive, electrophysiological, and morphological levels. Our unbiased proteomic profiling did not detect changes in canonical XBP1s-target genes involved in proteostasis or other direct downstream mediators from other branches of the UPR, as described in other organs, but rather revealed altered expression of a cluster of proteins related to synaptic function and neurodegenerative diseases. Many of the identified proteins, however, represent cargoes of the secretory pathway, suggesting that XBP1s overexpression does modulate neuronal proteostasis at least to some extent.

Although not evaluated here, we cannot exclude the possibility that targeting the IRE1/XBP1 pathway may impact other UPR branches during aging, contributing to the effects observed in neuronal function. In this line, genetic ablation of the PERK pathway altered cognitive function (Hughes & Mallucci, 2019; Krukowski *et al.*, 2020) and was previously explored in the dopaminergic system during aging (Sharma *et al.*, 2018). Moreover, pharmacological strategies to block the consequences of eIF2 $\alpha$  phosphorylation (the integrated stress response) improve cognitive function during aging (Krukowski *et al.*, 2020). In those lines, the role of PERK-eIF2 $\alpha$  in synaptic plasticity and memory consolidation has been extensively evaluated both in physiological and disease context (Lourenco *et al.*, 2013; Ma *et al.*, 2013; Trinh & Klann, 2013; Costa-Mattioli & Walter, 2020; Oliveira *et al.*, 2021). Interestingly, we show that impairment of UPR signaling start to take place during middle age, similar to findings in *C. elegans* (Ben-Zvi *et al.*, 2009) suggesting a cumulative disruption in proteostasis that eventually facilitates cognitive decline in advance age.

Importantly, accumulating evidence suggests that UPR mediators, and more specifically XBP1, exhibit alternative functions in the nervous system by controlling synaptic plasticity and dendritogenesis (Hayashi *et al.*, 2007; Martínez *et al.*, 2018; Saito *et al.*, 2018). Our results indicate that overexpression of XBP1s using a transgenic mouse model has a dramatic effect in preventing alterations at the

proteomic level, observing a correction in the aging proteome of over 70%. Furthermore, our unbiased analysis did not reveal abrupt changes in individual protein expression, but rather subtle alterations in clusters of related proteins that when collectively evaluated using functional enrichment approaches. Among the genes altered during aging that are modified by the IRE1/XBP1 pathway, we highlight proteins involved in synaptic function and hence cognition. Of note, XBP1s has been reported to modulate intracellular calcium dynamics in neurons, correlating with reduced neurotoxicity in a fly model of AD (Casas-Tinto *et al.*, 2011). We also recently showed that overexpression of XBP1s in the hippocampus of an AD mouse model improves cognitive function and LTP (Duran-Aniotz *et al.*, 2022). Along these lines, an imbalance in calcium homeostasis has long been proposed as a central player in neuronal aging (Gibson & Peterson, 1987). Our findings suggest that many proteins associated with calcium signaling in neurons, namely calcineurin, calmodulin, calcium transporter ATP2B4, and other cell signaling components, such as adenylyl cyclase, are modified following XBP1s overexpression in aged mice (Tables 3 and 4). Prior work has suggested that the improvement in LTP, dendritic spike stabilization, and memory formation in aged mice reported here are dependent on calcium homeostasis.

Additionally, we performed electrophysiological assessments in aged animals treated with AAV-XBP1s to measure the electrical properties of hippocampal pyramidal neurons under basal conditions and following PTX exposure to enhance excitatory properties. We found that XBP1s overexpression increases both firing rates and bursting activity after PTX treatment in addition to increasing postsynaptic excitatory potentials following theta burst stimulation in the aged hippocampus. However, basal firing rates and bursting activity were reduced in aged brain tissue overexpressing XBP1, suggesting compensatory or homeostatic changes associated with synaptic plasticity (Martínez *et al.*, 2018). Aging has been reported to correlate with altered GABAergic signaling, contributing to an imbalance in inhibitory/excitatory circuitry (Rozycka & Liguz-



**Table 4.** Table depicts most enriched terms in KEGG database comparing aged mice injected with AAV-Mock or AAV-XBP1s. Table indicates enriched terms and their associated genes. Symbols highlight whether enriched terms correlate with terms found during the natural course of aging in control animals.

Enriched terms	Genes
<b>Synaptic function</b>	
Endocrine calcium reabsorption <sup>a</sup>	CALB1;CLTB;CLTA
SNARE interactions in vesicular transport <sup>b</sup>	STX7;VAMP1
Long-term potentiation <sup>c</sup>	PPP3R1;CALM2
Synaptic vesicle cycle <sup>c</sup>	CLTB;CLTA
Endocytosis <sup>b</sup>	CLTB;CLTA;ASAP2; RAB11FIP2
Calcium signaling pathway <sup>c</sup>	PPP3R1;CALM2;SLC8A2
Glutamatergic synapse <sup>c</sup>	PPP3R1;GNG2
<b>Neurodegeneration</b>	
Prion diseases <sup>c</sup>	C1QB;C1QA;PRNP;LAMC1
Amyotrophic lateral sclerosis <sup>c</sup>	PPP3R1;NEFL;NEFM
Alzheimer disease <sup>c</sup>	APP;PPP3R1;NDUFV2; CALM2
Necroptosis <sup>b</sup>	HIST3H2A;H2AFY2;H2AFY;H2AFV
Huntington disease <sup>a</sup>	CLTB;TFAM;CLTA;NDUFV2
Cellular senescence <sup>c</sup>	PPP3R1;CALM2
Parkinson disease <sup>b</sup>	NDUFV2
<b>Metabolism/Bioenergetics</b>	
Glycolysis/Gluconeogenesis <sup>c</sup>	ENO1;ENO2
Glucagon signaling pathway <sup>c</sup>	PPP3R1;CALM2
Oxidative phosphorylation <sup>b</sup>	NDUFV2
Insulin signaling pathway <sup>c</sup>	CALM2
HIF-1 signaling pathway <sup>c</sup>	TRF;ENO1;ENO2
ECM-receptor interaction <sup>b</sup>	COL1A1;LAMA5;COL1A2;COL4A2;LAMA2; LAMB2;LAMB1;LAMC1;AGRN; HSPG2
RNA degradation <sup>c</sup>	ENO1;ENO2
Spliceosome	RBMXL1;SNRPD2;SNRPD1;TRA2B; SRSF1;PLRG1;SNRPB
Ribosome	RPL4;MRPS9;RPL31;RPL12;RPLP2;RPL19

<sup>a</sup>Term associated to Young WT x Middle-aged WT.

<sup>b</sup>Term associated to Middle-aged WT x Aged WT.

<sup>c</sup>Term associated to Young WT x Aged WT.

Lecznar, 2017). In line with this concept, a transcriptomic analysis of XBP1-deficient primary neuronal cultures revealed dysregulation of important GABAergic markers (Hayashi et al, 2008). Future studies will be needed to further define the possible regulation of GABA signaling by XBP1s in mammalian brain aging.

XBP1s has also been shown to control the transcription of BDNF (Martínez et al, 2016), and BDNF signaling is known to trigger XBP1 mRNA splicing (Hayashi et al, 2008; Martínez et al, 2016). Along these lines, we observed reduced *Bdnf* mRNA levels in the brain of IRE1<sup>CKO</sup> animals with aging (Fig EV5E), but no significant alteration in aged mice treated with AAV-XBP1s (Fig EV5F). Nonetheless, our unbiased proteomic profiling suggests a more complex, rich, and diverse effect of the UPR on brain physiology and healthspan. Prior reports have demonstrated

the involvement of the IRE1-XBP1s pathway in a variety of age-related neurodegenerative conditions, including PD/LBD, AD, ALS, FTD (Smith & Mallucci, 2016; Hetz & Saxena, 2017), and retinal degeneration in diabetes (McLaughlin et al, 2019). However, whether increased activity of the UPR could restore neuronal function in the context of normal mammalian aging in the absence of disease was not accessed prior to this report. Moreover, the mechanism driving brain aging versus neurodegenerative diseases is predicted to be different. Our proteomic profiling suggests that XBP1s overexpression modulates the expression of a variety of proteins related to several neurodegenerative diseases. These findings support the concept that targeting central components of the proteostasis network, such as the UPR, may influence the risk of developing these neurodegenerative disorders, in which XBP1 operates as an intersection between the biology of aging and the emergence of pathological protein misfolding.

Further along this line, a previous study suggested that XBP1s directly controls the expression of several AD-related genes (Acosta-Alvear et al, 2007), and a polymorphism in the *XBP1* promoter is a known risk factor for AD (Liu et al, 2013). Moreover, a recent exome-wide association analysis showed that a single-nucleotide polymorphism (SNP) in the *Ern1* gene (encoding IRE1 in humans) is associated with late-onset AD (He et al, 2021). Beyond proteostasis control, IRE1 may also influence AD progression by regulating amyloid precursor protein (APP) metabolism and amyloid- $\beta$  production (Duran-Aniotz et al, 2017). In agreement with this idea, several reports have indicated that the overexpression of proteostasis mediators is beneficial in animal models of neurodegenerative diseases (Martínez et al, 2018).

In addition to XBP1, IRE1 possesses other mRNA targets that can be cleaved in a process known as regulated IRE1-dependent decay of mRNA (RIDD) (Maurel et al, 2014). This process could contribute to the differences we observed in behavioral assessments between XBP1- and IRE1-null animals. In addition, studies in peripheral tissues have demonstrated that conditional deletion of XBP1 can trigger artificial phenotypes associated with IRE1 overactivation (Lee et al, 2008, 2011; Hur et al, 2012). This observation prompted us to focus our studies on IRE1 loss-of-function experiments to fully inactivate the pathway, and then use XBP1-deficient animals to validate the involvement of the linear IRE1/XBP1 pathway studied here. Collectively, our results support the idea that enhancing the IRE1/XBP1s pathway in the brain improves cognitive function during normal aging, and this finding has obvious therapeutic implications.

Studies of other model systems suggest that all UPR signaling branches can regulate the process of senescence (Abbadie & Pluquet, 2020). Here, we show that the normal appearance of senescent cells in the hippocampus with aging was prevented by XBP1s gene delivery, whereas IRE1 deficiency accelerated the emergence of senescent cells. The mechanisms behind such phenomena and the possible involvement of inflammatory mediators triggered in distinct cellular populations following senescent-associated phenotypes (SASP) should be addressed in future studies. Our results are consistent with a role of XBP1 as a modifier of aging phenotypes. In fact, other studies have suggested the occurrence of alterations in the UPR in elderly human tissue (Tang & Yang, 2015; Hart et al, 2019; Prell et al, 2019). Thus, strategies to improve ER proteostasis or boost the adaptive activity of the UPR might be

useful in extending human brain health span, reducing the risk of developing dementia and other age-associated neurodegenerative diseases. Interestingly, a large-scale proteomic human study identified promising protein targets that may help sustain cognitive stability during aging (Wingo *et al*, 2019), and suggested that myelin-associated proteins and neurofilaments are associated with cognitive resilience. These findings overlap with our proteomic profiling, suggesting that the UPR may modify similar pathways (Tables 3–4; Fig EV4D). Additionally, altered expression of extracellular matrix component laminin-A and glial fibrillary-associated protein (GFAP), two proteomic hits highlighted in our analysis, have also been linked to resilience from cognitive impairment in studies on two human cohorts (Wingo *et al*, 2019; Tables 3–4; Fig EV4D). Moreover, analysis of human datasets indicated that some of the proteins restored by XBP1s overexpression in our murine model during aging are also altered in human brains during aging (Fig 4D).

Finally, the use of invertebrate models (e.g., yeast, *C. elegans* and *D. melanogaster*) has uncovered a central role of ER proteostasis and the UPR in aging (Martínez *et al*, 2018; Schinzel *et al*, 2019; Daniele *et al*, 2020; Taylor & Hetz, 2020). The positive consequences of activating neuronal and glial UPR on the life span of worms have been shown to involve global control of organismal proteostasis through a cell-nonautonomous mechanism (Wang *et al*, 2015; Luis *et al*, 2016; Imanikia *et al*, 2019; Frakes *et al*, 2020; Taylor & Hetz, 2020). Interestingly, the beneficial effects of caloric restriction, a major intervention that extends life span, was also linked to modulatory effects on ER proteostasis in invertebrate (Henis-Korenblit *et al*, 2010; Matai *et al*, 2019). It remains to be determined whether an increase in XBP1s expression in the aged brain can be translated into the propagation of adaptive signals that improve the function of other organs, thus mitigating their deterioration during normal aging.

## Materials and Methods

### Experimental design

This study aimed to test the role of the IRE1-XBP1s pathway in mediating mammalian brain aging. We first identified this pathway to be correlated with dementia emergence in a human cohort population. Next, we evaluate different cohorts of transgenic mice in gain and loss-of function mutations impacting IRE1-XBP1s pathway in the brain using behavioral, morphological, and proteomic approaches during aging. Finally, we treated aged WT animals with adeno-associated virus to manipulate XBP1s levels in the brain to test possible improvements in cognition and the reversal of age-associated phenotypes.

### Human study population

RNA-seq human data were extracted from The Aging, Dementia and Traumatic Brain Injury Study (<https://aging.brain-map.org/overview/home>) which is a detailed neuropathologic, molecular, and transcriptomic characterization of brains of control and TBI exposure cases from a unique aged population-based cohort from the Adult Changes in Thought (ACT) study. Differential gene expression in RNA-seq was performed directly by the website comparing

all donors clinically diagnosed as “Non demented” ( $n = 49$ ) versus “Dementia, type unknown,” “Possible Alzheimer’s disease,” “Probable Alzheimer’s disease” ( $n = 42$ ) irrespective to sex, years of education, TBI or pathological markers of AD pathology. Only minimum of 30 M 50 bp paired-end reads per sample were considered. A fold change cutoff  $> 1.2$ -fold was implemented in the gene list (FDR  $< 0.5$ ) to further functional enrichment analysis evaluation. Values are plotted as Fragments Per Kilobase Million (FPKM).

### Animals

C57BL/6 mice were employed, maintained in a facility with 12 h light/dark cycle at 25°C with food and water provided *ad libitum*. Cohorts of aged, middle-aged, and young animals were directly obtained from the Jackson’s Laboratory (USA). Different colonies of transgenic mice were generated in house (all in the C57BL/6 background) and are indicated in Appendix Fig S1. All animal procedures were approved by the Bioethics Committee of the Faculty of Medicine, University of Chile (protocol number 18166-MED-UCH).

### Stereotaxic injections

Young (3-month-old), middle-aged (12 month-old), and aged (18 month-old) mice received bilateral stereotaxic injections of AAV ( $1 \times 10^9$  viral genomes (VGs)/ $\mu$ l) in the hippocampi using the coordinates AP:  $-1.9$ , DV:  $+1.7$ , and ML:  $\pm 1.0$ . Male mice were deeply anesthetized using isoflurane (4%), and a stereotaxic apparatus coupled to a Hamilton microsyringe was used for the procedure. Cranium was exposed through a skin incision, and bilaterally symmetrical holes were opened using a dental drill. Injections were performed at approximately 0.5  $\mu$ l/min in a total of 1  $\mu$ l. Mice were returned to their home cages and kept under close monitoring until they were awake. Mice were injected with either control AAV serotype 2 vector (Mock) expressing eGFP (Addgene, #49055-AAV2), AAV2-CRE (Addgene, #105545-AAV2), or AAV2-XBP1s (produced at Genzyme by Pablo Sardi) under the control of the CMV promoter, in addition to an eGFP cassette to monitor transduction efficiency, as we previously reported (Valdés *et al*, 2014). For intracerebral injections with tunicamycin or vehicle, the same protocol was applied.

### Behavioral assessment design

Behavioral experiments were performed in a blinded manner, both for genetically modified animals and AAV-injected mice, using groups of age-matched controls. Both males and females were evaluated for all tests in transgenic colonies in a balanced fashion. For AAV-based experiments, only males were used due to logistic and experimental limitations. Injected mice underwent behavioral evaluation 3–4 weeks following injections. Assessments were designed in line with bioethical guidelines restricting the total number of animals used in the study, thus prohibiting us to use separated cohorts for each behavioral task in this study and are indicated as follows.

### IRE1<sup>CKO</sup> colony

Young, middle-aged, and aged animals were evaluated in the following order: Novel Object Recognition (NOR) and Novel Object Location (NOL) tests. Additional cohorts of young, middle-aged, and

aged animals were evaluated only in the contextual fear conditioning (CFC) test (Appendix Fig S2). Re-evaluation in different points of aging was only performed in the NOR tests and did not impact animals' performance (Fig EV1L).

### **Tg<sup>XBP1s</sup> colony**

Young, middle-aged, and aged animals were evaluated in the following order: NOR and NOL tests. Aged animals were further evaluated in the Barnes maze test. Two additional cohorts of young and middle-aged mice were evaluated only in the Barnes maze test. Additional cohorts of young, middle-aged, and aged animals were evaluated only in the CFC (Appendix Fig S3). Re-evaluation in different points of aging was only performed in the NOR and NOL tests and did not impact animals performance (Fig EV1L).

### **AAV-XBP1s or mock WT-treated colony**

Middle-aged and aged WT animals treated with AAV-XBP1s or AAV-Mock were evaluated in the following order: NOR and NOL tests. A cohort of aged animals injected with AAV-XBP1s or AAV-Mock was further evaluated in the Barnes maze and then in the CFC test. In this paradigm, animals were never re-evaluated in the same test (Appendix Fig S4).

### **Middle-aged IRE1<sup>CKO</sup> colony treated with AAV-Cre or AAV-XBP1s**

Young or middle-aged IRE1<sup>CKO</sup> or IRE1<sup>flox/flox</sup> animals were only evaluated in the NOR test before and after treatment with corresponding AAV (Appendix Fig S5).

## **Behavioral tests description**

### **Novel object recognition**

Novel object recognition (NOR) was performed as previously described (Leger *et al*, 2013; Vogel-Ciernia & Wood, 2014). Briefly, mice were first trained and then placed in an arena facing the wall. They were presented with two identical objects (Lego blocks, 3 × 4 cm) located in a distal position toward the animal. For the training phase, mice were allowed to explore both objects for a total time of exploration of 20 s during a single trial. If exploration did not occur within 20 s, a maximum time of 5 min was given for each animal to explore the objects. After 24 h, mice were again placed in the arena facing the wall but at this time were introduced to a new object of different color, shape, and texture. Following 24 h, in the test phase, mice were again allowed to explore objects for a maximum of 20 s or 5 min if the criterion of exploration was not accomplished in the initial time allotment. Four different Lego blocks with equivalent sizes (3–4 × 4 × 4 cm) were presented in a randomized fashion for each animal. Trials were recorded on a digital camera coupled to a computer for subsequent evaluation of interaction time exploring objects by a blinded researcher. Both the objects and the arena were cleaned with 70% ethanol before each session to avoid olfactory cues. Exploration time was defined as the amount of time mice had their noses oriented toward an object with its nose within 3 cm or less. Other behaviors such as rearing near the object or resting against the object were not considered as exploration. Exploration time spent during the training phase was also recorded. Animals that failed to interact with one or both objects in the training phase, or that showed signs of distress were excluded from the analysis. Animals that spent 100% of time of exploration in the

same object both in the training and in the test days were also excluded from the analysis. All analyses were performed in a masked fashion. Results were plotted as an index of the difference in exploration time between novel and familiar objects divided by the total amount of exploration time of both objects.

### **Novel object location**

The novel object location (NOL) task was performed as previously described (Leger *et al*, 2013; Vogel-Ciernia & Wood, 2014). Mice were placed in the same arena used for the NOR assay. The arena was divided into quadrants. For the training phase, mice were introduced to two identical objects (Lego blocks, 5 × 4 × 4 cm) placed in two randomized quadrants of the arena. Objects were placed equidistant from one other. At 3 or 24 h after the test phase, mice were again placed in the arena facing the wall but now with one of the objects placed in a distinct quadrant. Trials were recorded on a digital camera coupled to a computer for subsequent evaluation of interaction time exploring objects. Both the objects and the arena were cleaned with 70% ethanol before each session to avoid olfactory cues. Exploration time was defined as the amount of time mice had their noses oriented toward an object with its nose within 3 cm or less. As per standard protocol, animals that failed to interact with one or both objects or showed signals of stress were excluded from the analysis. Animals that failed to interact with one or both objects in the training phase, or that showed signs of distress were excluded from the analysis. Animals that spent 100% of time of exploration in the same quadrant both in the training and in the test days were also excluded from the analysis. All analyses were performed in a masked fashion. Results were plotted as an index of the difference in exploration time between novel located and familiar objects divided by the total amount of exploration time of both objects.

### **Barnes maze**

The Barnes maze task was performed on a white circular surface (0.9 m in diameter) with 20 holes equally spaced around the perimeter, as previously described (Sunyer *et al*, 2007). A dark escape box (10 × 20 × 7.8 cm) was located under one of the holes, which was the target. A ramp was placed under the target hole so that mice could reach the escape tunnel easily. The circular open field was elevated 75 cm above the floor. Distal spatial cues (with different colors and shapes) were placed outside of the maze. The maze was rotated daily, with the spatial location of the target unchanged with respect to the distal visual room cues. A cylindrical start chamber was placed in the center of the maze and removed after 10 s. Training sessions consisted of four trials per day conducted for 4 days with a maximum of 3 min each. If animals were unable to find the target after 3 min, they were gently placed in the right hole by the tail. A stopwatch sound was used as an aversive stimulus to induce exploration. Once a mouse reached the target, the noise was immediately stopped, and the mouse was left inside the box for 1 min and then returned to its home cage. A minimal period of 15 min was given for the intertrial interval for each animal. The maze and the escape box were cleaned with 70% ethanol between each trial to avoid olfactory cues. The numbers of primary pokes and the primary latency to reach the target were manually counted, as defined by the number of pokes and time to reach the target for the first time, as some animals did not promptly enter the escape box during training sessions. Every trial was recorded on a video camera placed

in the ceiling and fed to a computer. On the fifth day, the escape box was removed, and one single trial was performed as a probe trial to evaluate spatial memory acquisition with a maximum time of 90 s. The fifth day is referred here as the “test day.”

### Contextual fear conditioning

On the acquisition day (Day 1), mice were placed in the contextual fear conditioning chamber (Med Associates) and during the first minute, no stimulus was applied. Then, 80 db of white noise was generated for 30 s followed by a 2 s 0.5 mA electric shock. After the shock, mice were let in the cage for one more minute. Freezing episodes and freezing responses (represented by the percentage of freezing response to total activity) were measured by an automated system (Med Associates). Following 24 h, on the retention day (Day 2) mice were again placed in the same chamber and exposed to the same protocol but this time without any electroshock. Freezing events and freezing percentage time were recorded for 3 min. Mice that displayed excessive signs of stress, harm, or discomfort were excluded from the experiment. Mice that did not move in acquisition and retention days or that displayed clear signs of altered mobility were excluded from the analysis.

### Tissue collection and processing

Briefly, mice were deeply anesthetized with ketamine/xylazine and perfused with ice-cold saline. The brain was removed from the skull and separated into two hemispheres. The hippocampus, cerebral cortex, and cerebellum of the left hemisphere were dissected out and stored frozen at  $-80^{\circ}\text{C}$  until analysis. The right hemisphere was postfixed in 4% paraformaldehyde in PBS overnight at  $4^{\circ}\text{C}$ , followed by cryopreservation in 30% sucrose in PBS and freezing medium (OCT, TissueTek). Subsequently, 40  $\mu\text{m}$ -thick sagittal sections were obtained free-floating on a Leica cryostat for immunostaining using anti-NeuN (Millipore, MAB377, 1:100) to label neurons. Five serial sections every 200  $\mu\text{m}$  were stained per animal. Fluorescence images were acquired using a confocal microscope (Nikon C<sup>2+</sup>).

### Dendritic spine imaging

Brain slices were cut at 40- $\mu\text{m}$  thickness on a cryostat. AAV2-GFP fluorescence was previously confirmed in injected animals to validate viral transduction using an inverted epifluorescence microscope and then imaged on a confocal microscope, Nikon Eclipse T1, at 60 $\times$  magnification with additional digital zoom of 3 $\times$ . Similar regions were compared among animals (CA1 region, spines in primary and secondary dendrites between the *stratum radiata* and the pyramidal layer, AP:  $-1.9$  to  $-2.1$  from the bregma). Z-stacks were acquired in 0.5- $\mu\text{m}$  slices, laser intensity at 0.5–1% and 12.5  $\mu\text{s}$ /pixel at 1024  $\times$  1024 resolution. Z-Stacks were then summed using ImageJ software for total maximum intensity to generate one single stacked 8-bit image. The number of spines was manually quantified in scaled images and divided by the length of the dendrite analyzed; 5–10 dendrites per animal were used for analysis.

### Immunofluorescence

Brain slices were incubated in citrate buffer at  $96^{\circ}\text{C}$  for 30 min for epitope exposition and washed in PBS. After this, slices were

washed in TBS and incubated in blocking solution (3% BSA and 0.05% Triton X-100) for 60 min at room temperature. Slices were then incubated overnight at  $4^{\circ}\text{C}$  with primary antibody anti-phospho-Histone H2AX Ser139 (Sigma-Aldrich, 05-636) diluted 1:1,000 in 3% BSA in TBS. Secondary antibody was Alexa Fluor 568 (Invitrogen A-11031) diluted 1:2,000 in 3% BSA in TBS. The samples were washed three times using TBS, and in the final wash, DAPI was added and incubated for 5 min. Images were taken with Leica TCS SP8 confocal microscope with a 40 $\times$  objective magnification. ImageJ and LAS X software were used to process the stacked images. The percentage of positive cells for p-H2AX was graphed. Representative images are shown.

### Senescence-associated beta-galactosidase (SA- $\beta$ gal) staining

Histochemical detection of SA- $\beta$ gal activity was performed as previously reported (Debacq-Chainiaux *et al.*, 2009). Briefly, slices were incubated in a 1 mg/ml of solution of 5-bromo-4-chloro-3-indolyl  $\beta$ -D-galactopyranoside in 0.04 M citric acid/sodium, 0.005 M  $\text{K}_3\text{Fe}(\text{CN})_6$ , 0.005 M  $\text{K}_4\text{Fe}(\text{CN})_6$ , 0.15 M NaCl and 0.002 M  $\text{MgCl}_2$ , and diluted in phosphate-buffered saline (pH 6) for 16 h. After incubation, slices were washed with TBS and mounted on superfrost microscope slides (ThermoFisher 6776214) using Fluoromount-G (ThermoFisher, 00-4958-02). One slice per animal was used, and all slices were processed at the same time. Images were acquired on a Leica DM500 binocular microscope equipped with a Leica ICC50 W camera using 4 $\times$  and 10 $\times$  objective magnifications. ImageJ software was used to process the images. Positive area for SA- $\beta$ gal activity was measured and representative images are shown.

### FluoroJade-C staining

Brain sections were incubated in 0.06% potassium permanganate solution for 10 min. Next, sections were incubated in 0.0001% of Fluoro-Jade C solution and washed three times with distilled water and incubated with DAPI for 5 min. Images were acquired using Olympus XI spinning disk microscope (10 $\times$  magnification). ImageJ software was used to process images and evaluate integrated density of hippocampal area.

### Electrophysiological measurements

#### Excitatory postsynaptic field recordings

Hippocampal slices were prepared as we previously reported (Ardiles *et al.*, 2012; Ravello *et al.*, 2019). Briefly, mice were deeply anesthetized with isoflurane (Forene B506 AbbVie), brains quickly removed, and hippocampi sectioned into 300- $\mu\text{m}$ -thick slices in ice-cold dissection buffer (in mM: 2.6 KCl, 1.23  $\text{NaH}_2\text{PO}_4$ , 26  $\text{NaHCO}_3$ , 212.7 sucrose, 10 dextrose, 3  $\text{MgCl}_2$ , and 1  $\text{CaCl}_2$ , equilibrated with 95%  $\text{O}_2$  and 5%  $\text{CO}_2$ ) using a vibroslicer (Leica VT1200S, Leica Microsystems, Nussloch, Germany). Slices recovered for 1 h at room temperature in an artificial cerebrospinal fluid (ACSF, in mM: 124 NaCl, 5 KCl, 1.25  $\text{NaH}_2\text{PO}_4$ , 26  $\text{NaHCO}_3$ , 10 dextrose, 1.5  $\text{MgCl}_2$ , and 2.5  $\text{CaCl}_2$  bubbled with a mixture of 5%  $\text{CO}_2$  and 95%  $\text{O}_2$ ) and then transferred to a submerged recording chamber superfused with ACSF ( $30^{\circ}\text{C}$ , 2 ml/min). Synaptic responses were evoked with 0.2 ms pulses delivered through theta glass micropipettes (TG200-4, Warner Instruments) filled with ACSF, and



extracellularly recorded in the stratum radiatum of CA1. Baseline responses were recorded at 0.033 Hz using a stimulation intensity that evoked a half-maximal response, defined as the maximal response without a population spike (pop-spike). Slices were discarded if the postspike appeared in the initial rising phase, paired-pulse facilitation at a 50 ms interval was < 10%, or the baseline was not stable. LTP was induced using theta burst stimulation (TBS; 10 trains of four pulses each at 100 Hz; 5 Hz interburst interval) delivered at 0.1 Hz. LTP magnitude was calculated as the average (normalized to baseline) of the responses recorded 50–60 min after conditioning stimulation.

### Multielectrode array (MEA) recording

Hippocampal slices were used to record extracellular spikes and local field potentials (Multielectrode arrays [MEA] 252 electrodes, Multichannel Systems). Hippocampal slices were mounted on a MEA matrix bathed in an ACSF medium (in mM: NaCl 125, KCl 2.5, glucose 25, NaHCO<sub>3</sub> 25, NaH<sub>2</sub>PO<sub>4</sub> 1.25, CaCl<sub>2</sub> 2, and MgCl<sub>2</sub> 1) at 32°C and constantly bubbled with 95% O<sub>2</sub> and 5% CO<sub>2</sub>. We used a spike sorting algorithm (Spyking-Circus, <http://www.yger.net/software/spyking-circus>) to separate and individualize each recorded neuron. The steps consisted of filtering the raw extracellular traces, whitened them (to remove correlated noise), clustering the action potential waveforms, and fitting them to the whitened traces.

### Firing and burst rate recordings

Firing rate was computed as the number of spikes divided by the recording length using Neuroexplore (<https://www.neuroexplorer.com/>) software. Burst rate analysis was computed by an interspike interval routine implemented by a custom Matlab procedure (Chen et al, 2009). Spontaneous activity (SA) was recorded for 10 min, following a 30-min application of picrotoxin (PTX, 100 μM).

### Biochemical and molecular analysis

Total tissue RNA was extracted using Trizol™ Reagent (Invitrogen) according to the manufacturer's instruction. cDNA was synthesized with random primers using a High-Capacity cDNA Reverse Transcription KIT (Applied Biosystems) and subsequently subjected to quantitative PCR analysis using HOT FIREPol® EvaGreen® qPCR Mix plus (ROX) (Solis Bio Dyne) on a Stratagene Mx3000P machine (Agilent Technologies). Actin mRNA expression was used to normalize all samples. The sequences of primers used were as follows:

Gene	Forward primer	Reverse primer
<i>Xbp1s</i>	TGC TGA GTC GGC AGC AGG TG	GAC TAG CAG ACT CTG GGG AAG
<i>Hspa5</i>	TCA TCG GAC GCA CTT GGA A	CAA CCA CCT TGA ATG GCA AGA
<i>Ddit3</i>	TGG AGA GCG AGG GCT TTG	GTC CCT AGC TTG GCT GAC AGA
<i>Ern1</i>	CCG AGC CAT GAG AAA CAA GAA	GGG AAG CGG GAA GTG AAG TAG.
<i>Actin</i>	TAC CAC CAT GTA CCC AGG CA	CTC AGG AGC AAT GAT CTT

<i>Bdnf</i>	CCT GCA TCT GTT GGG GAG AC	GCC TTG TCC GTG GAC GTT TA
<i>exon1</i>		
<i>Atf3</i>	CAGACCCCTGGAGATGTCACT	TTCTTGTTTCGACACTTGGCA
<i>Pdia3</i>	GGTGATCACAGCTGGACTA	GGACTCACATTGGTCCA TGCACACCTA
<i>Bloc1s1</i>	GAA CTG GGC TAG GAG CAT CG	ATT CGT GGC TCA CCA GTT TCC

### Detection of S-nitrosylated (SNO-)IRE1 and total IRE1 levels

We performed biotin-switch assays using whole-brain tissue samples as previously described with minor modifications (Uehara et al, 2006). Briefly, brain tissue extracts were prepared in 400 μl HEN-RIPA buffer (100 mM Hepes pH 7.5, 1 mM EDTA, 0.1 mM neocuproine, 150 mM NaCl, 1% NP-40, 0.5% sodium deoxycholate, and 0.1% SDS) containing a thiol blocking reagent (20 mM methyl methanethiosulfonate [MMTS]) in a 3 ml homogenizer. After centrifuging to remove tissue debris, SDS was added to each sample to a final concentration of 1%. Samples were then incubated for 30 min at 42°C to block free thiol groups. After removing excess MMTS by acetone precipitation, S-nitrosothiols were reduced to thiols with 10 mM ascorbate. The newly formed thiols were then linked with the sulfhydryl-specific biotinylating reagent N-[6-(biotinamido)hexyl]-3'-(2'-pyridyldithio)propionamide (Biotin-HPDP). The biotinylated proteins were pulled down with Streptavidin-agarose beads, and Western blot analysis performed to detect SNO-IRE1 (1:1,000, Cell Signaling 3294S). To monitor the amount of "input" protein by immunoblot, a 20 μl aliquot of the sample was saved prior to the step of Streptavidin-agarose bead addition in the biotin-switch assay. Total IRE1 was monitored by quantitative densitometry of standard immunoblot assays. GAPDH was monitored as a control to ensure equal loading (1:1,000, Millipore MAB374).

### Quantitative proteomic analysis

The hippocampi of male mice transgenic, nontransgenic, or transduced with AAV2 (Mock or XBP1s) were homogenized in TEN buffer (10 mM Tris-HCl pH 8.0, 1 mM EDTA, 100 mM NaCl, 1% NP-40) and protein inhibitor cocktail (Roche), and then sonicated for 15 s at 30% amplitude (QSonica). For each sample lysate, 20 μg was precipitated with chloroform/methanol. Samples for mass spectrometry analysis were prepared as described (Plate et al, 2016). Air-dried pellets were resuspended in 1% RapiGest SF (Waters) and diluted to final volume in 100 mM HEPES (pH 8.0). Proteins were reduced with 5 mM Tris(2-carboxyethyl)phosphine hydrochloride (Thermo Fisher) for 30 min and alkylated with 10 mM iodoacetamide (Sigma-Aldrich) for 30 min at room temperature in the dark. Proteins were then digested for 18 h at 37°C with 0.5 μg trypsin (Promega). After digestion, the peptides from each sample were reacted for 1 h with the appropriate tandem mass tag (TMT) isobaric reagent (Thermo Fisher) in 40% (v/v) anhydrous acetonitrile and quenched with 0.4% ammonium bicarbonate for 1 h. Samples with different TMT labels were pooled and acidified with 5% formic



acid. Acetonitrile was evaporated on a SpeedVac and debris removed by centrifugation for 30 min at 18,000 g. MudPIT microcolumns were prepared as described (Ryno *et al*, 2014). Liquid chromatography–tandem mass spectrometry (LC-MS/MS) analysis was performed using a Q-Exactive HF mass spectrometer equipped with an Ultimate 3000 nLC 1000 (Thermo Fisher). MudPIT experiments were performed by 10  $\mu$ l sequential injections of 0, 10, 20, 30, ..., 100% buffer C (500 mM ammonium acetate in buffer A) and a final step of 90% buffer C/10% buffer B (100% acetonitrile, 0.1% formic acid, v/v/v), with each step followed by a gradient from buffer A (95% water, 5% acetonitrile, 0.1% formic acid) to buffer B. Electrospray was performed directly from the analytical column by applying a voltage of 2.2 kV with an inlet capillary temperature of 275°C. Data-dependent acquisition of MS/MS spectra was performed with the following settings: Eluted peptides were scanned from 300 to 1,800  $m/z$  with a resolution of 120,000. The top 15 peaks for each full scan were fragmented by higher energy collisional dissociation (HCD) using a normalized collision energy of 38%, isolation window of 0.7  $m/z$ , a resolution of 45,000, AGC target  $1e5$ , maximum IT 60 ms, and scanned from 100 to 1,800  $m/z$ . Dynamic exclusion was set to 10 s. Peptide identification and protein quantification was performed using Proteome Discoverer 2.4 (ThermoFisher). Spectra were searched using SEQUEST against a UniProt mouse proteome database. The database was curated to remove redundant protein and splice-isoforms, and common contaminants were added. Searches were carried out using a decoy database of reversed peptide sequences using Percolator node for filtering and the following settings: 10 ppm peptide precursor tolerance, 6 amino acid minimum peptide length, trypsin cleavage (maximum 2 missed cleavage events), static Cys modification of 57.021517 (carbamidomethylation), and static N-terminal and Lys modification of 229.1629 (TMT-sixplex), FDR 0.01, 2 peptide IDs per protein. Normalization of TMT reporter ion intensities was carried out based on total peptide abundance in each channel, and subsequently, TMT ratios for each identified protein were calculated in reference to a common pooled sample. Finally, the scaled, reference-normalized TMT intensities were compared between young WT and XBP1s Tg ( $n = 4, 4$ ), middle-aged WT and XBP1s Tg ( $n = 3, 4$ ) and aged WT and Tg<sup>XBP1s</sup> ( $n = 3-4$ ) or aged injected with AAV-Mock ( $n = 4$ ) or AAV-XBP1s ( $n = 5$ ) and significance was assessed using a background based *t*-test with multiple testing correction in the Reporter Ions Quantifier node (Benjamini *et al*, 2006). Significantly altered genes were filtered by considering a cutoff of FDR < 0.1 irrespective to fold change between groups (Dalman *et al*, 2012). Keratins and other common contaminants were excluded from further analyses (Hodge *et al*, 2013). Proteins where TMT intensities were absent in more than one sample per group were also excluded. Gene set enrichment analysis was performed in EnrichR or STRING platforms using Kyoto Encyclopedia for Genes and Genomes (KEGG) and Gene Ontology annotations (Kuleshov *et al*, 2016; Szklarczyk *et al*, 2019). Heatmaps and hierarchical clustering were generated using Morpheus (<https://software.broadinstitute.org/morpheus>).

The correlation between the results from the differential proteomics analysis was calculated using Spearman's method on log-fold changes. To identify proteins leading the reversal of the aging-related changes by XBP1s, we ranked the proteins from the most downregulated to the most upregulated during aging, and from the

most up-regulated to the most downregulated by XBP1s. Then we calculated the rank product of each protein based both ranking lists. Top 50 proteins with the highest and lowest rank product were selected for the downstream comparison with human aging. To identify proteins changing with aging in humans, we used transcriptomic data from human hippocampus from Kang *et al* (2011), Berchtold *et al* (2008) and GTEX v8 (<https://gtexportal.org/home>). We calculated Spearman's correlation between the log-transformed normalized expression values and the age of the samples. Mouse orthologs of the human genes were obtained using the WORMHOLE ortholog prediction web tool with default parameters (Sutphin *et al*, 2016).

### Statistical analysis

Statistical significance was queried with Student's *t*-test or Kolmogorov–Smirnov test for single comparisons and for multiple comparisons with simple or repeated measurements one-way or two-way ANOVA, followed by Holm–Sidak's post hoc test, depending on experimental design. *P*-values were considered significant when they were < 0.05. Number of animals and *P*-values are discriminated in each graph legend. *P*-values computed by two-way ANOVA indicating source of variation between variables are reported in figure legends.

### Data availability

The mass spectrometry proteomics data have been deposited to the ProteomeXchange Consortium via the PRIDE (Perez-Riverol *et al*, 2019) partner repository with the following details:

Project Name: Contribution of the Unfolded Protein Response (UPR) transcription factor XBP1 to brain aging; Project accession: PXD020539.

Additionally, all information is available in Dataset EV2.

Expanded View for this article is available online.

### Acknowledgments

We thank Dr. Takao Iwawaki for providing IRE1 $\alpha$  null animals. We thank Javiera Ponce, Francisco Aburto and Diego Rivas for animal care. We also thank Monica Flores and Maria Painavel for technical support. FONDECYT 1220573 (CH). FONDAP program 15150012 (CH). Millennium Institute Initiative P09-015-F and P09-022-F (CH). European Commission R&D MSCA-RISE 734749 (CH). FONDEF ID16110223 (CH) and ID22110120. Department of Defense USA grant W81XWH2110960 PD200085 (CH). U.S. Air Force Office of Scientific Research grant FA9550-16-1-0384 (CH). Comisión Nacional de Investigación Científica y Tecnológica (CONICYT)-CNP1q 441921/2016-7 (CH). FONDECYT 1170614 (JPH). FONDECYT 11160760 (CDA). Postdoctoral fellowships: FONDECYT 3180195 (FCM) and FONDECYT 3080702 (YG), 3190596 (MLD), 1191003, and 1191538. Conicyt - RED1170583 (CDA). FONDECYT 11150776 (AOA). FONDECYT (RV). NIH: R35 AG071734, R01 NS086890, R01 DA048882, DP1 DA041722, RF1 AG057409, and R01 AG056259 (to SAL), R01 AG061845 (to TN), R35 GM133552 (to LP).

### Author contributions

**Felipe Cabral-Miranda:** Conceptualization; data curation; formal analysis; funding acquisition; investigation; visualization; methodology; writing –

original draft; project administration; writing – review and editing. **Giovanni Tamburini:** Data curation; formal analysis; investigation; methodology. **Gabriela Martinez:** Formal analysis; funding acquisition; investigation; methodology. **Alvaro O Ardiles:** Formal analysis; funding acquisition; visualization; methodology. **Daniilo B Medinas:** Formal analysis; funding acquisition; investigation; methodology. **Yannis Gerakis:** Formal analysis; investigation; methodology. **Mei-Li Diaz Hung:** Formal analysis; funding acquisition; investigation; methodology. **René Vidal:** Formal analysis; methodology. **Matias Fuentealba:** Formal analysis; investigation; methodology. **Claudia Duran-Aniotz:** Formal analysis; funding acquisition; investigation; methodology. **Tim Miedema:** Formal analysis; investigation. **Javier Diaz:** Formal analysis; investigation; methodology. **Cristobal Ibaceta-Gonzalez:** Formal analysis; supervision; funding acquisition; methodology. **Carleen M Sabusap:** Formal analysis; investigation; methodology. **Francisca Bermedo-Garcia:** Formal analysis; investigation; methodology. **Paula Mujica:** Formal analysis; investigation; methodology. **Stuart Adamson:** Formal analysis; investigation; methodology. **Kaitlyn Vitangcol:** Formal analysis; investigation; methodology. **Hernan Huerta:** Formal analysis; investigation; methodology. **Xu Zhang:** Data curation; formal analysis; investigation; methodology. **Tomohiro Nakamura:** Formal analysis; investigation; methodology. **Sergio Pablo Sardi:** Funding acquisition; investigation; methodology. **Stuart A Lipton:** Data curation; formal analysis; supervision; funding acquisition; investigation; methodology. **Brian K Kennedy:** Formal analysis; funding acquisition; investigation; methodology. **Juan Pablo Henriquez:** Formal analysis; supervision; investigation; methodology. **Julio Cesar Cárdenas:** Formal analysis; funding acquisition; investigation; methodology. **Lars Plate:** Formal analysis; supervision; funding acquisition; investigation; methodology. **Adrian G Palacios:** Data curation; formal analysis; supervision; funding acquisition; investigation. **Claudio Hetz:** Conceptualization; resources; supervision; funding acquisition; investigation; writing – original draft; project administration; writing – review and editing.

## Disclosure and competing interests statement

CH and FCM declare a conflict of interest for a submitted patent application. Inventors: Claudio Hetz, Felipe Cabral Miranda. Title: Treatment of aging or age-related disorders using XBP1. Provisional application for patent at USPTO, application number 62800229. Submitted 01/02/2019. Status: patent pending. Disclosure: PS is a Sanofi employee. All other authors declare they have no competing interests.

## References

- Abbadie C, Pluquet O (2020) Unfolded protein response (UPR) controls major senescence hallmarks. *Trends Biochem Sci* 45: 371–374
- Acosta-Alvear D, Zhou Y, Blais A, Tsikitis M, Lents NH, Arias C, Lennon CJ, Kluger Y, Dynlacht BD (2007) XBP1 controls diverse cell type- and condition-specific transcriptional regulatory networks. *Mol Cell* 27: 53–66
- Ardiles AO, Tapia-Rojas CC, Mandal M, Alexandre F, Kirkwood A, Inestrosa NC, Palacios AG (2012) Postsynaptic dysfunction is associated with spatial and object recognition memory loss in a natural model of Alzheimer's disease. *Proc Natl Acad Sci USA* 109: 13835–13840
- Baker DJ, Petersen RC (2018) Cellular senescence in brain aging and neurodegenerative diseases: evidence and perspectives. *J Clin Invest* 128: 1208–1216
- Benjamini Y, Krieger AM, Yekutieli D (2006) Adaptive linear step-up procedures that control the false discovery rate. *Biometrika* 93: 491–507
- Ben-Zvi A, Miller EA, Morimoto RI (2009) Collapse of proteostasis represents an early molecular event in *Caenorhabditis elegans* aging. *Proc Natl Acad Sci USA* 106: 14914–14919
- Berchtold NC, Cribbs DH, Coleman PD, Rogers J, Head E, Kim R, Beach T, Miller C, Troncoso J, Trojanowski JQ et al (2008) Gene expression changes in the course of normal brain aging are sexually dimorphic. *Proc Natl Acad Sci USA* 105: 15605–15610
- Brown MK, Chan MT, Zimmerman JE, Pack AI, Jackson NE, Naidoo N (2014) Aging induced endoplasmic reticulum stress alters sleep and sleep homeostasis. *Neurobiol Aging* 35: 1431–1441
- Casas-Tinto S, Zhang Y, Sanchez-Garcia J, Gomez-Velazquez M, Rincon-Limas DE, Fernandez-Funez P (2011) The ER stress factor XBP1s prevents amyloid-beta neurotoxicity. *Hum Mol Genet* 20: 2144–2160
- Chen L, Deng Y, Luo W, Wang Z, Zeng S (2009) Detection of bursts in neuronal spike trains by the mean inter-spike interval method. *Prog Nat Sci* 19: 229–235
- Costa-Mattioli M, Walter P (2020) The integrated stress response: from mechanism to disease. *Science* 368: eaat5314
- Dalman MR, Deeter A, Nimishakavi G, Duan ZH (2012) Fold change and p-value cutoffs significantly alter microarray interpretations. *BMC Bioinformatics* 13: 1–4
- Daniele JR, Higuchi-Sanabria R, Durieux J, Monshietehadi S, Ramachandran V, Tronnes SU, Kelet N, Sanchez M, Metcalf MG, Garcia G et al (2020) UPRER promotes lipophagy independent of chaperones to extend life span. *Sci Adv* 6: eaaz1441
- Debaqç-Chainiaux F, Erusalimsky JD, Campisi J, Toussaint O (2009) Protocols to detect senescence-associated beta-galactosidase (SA-βgal) activity, a biomarker of senescent cells in culture and in vivo. *Nat Protoc* 4: 1798–1806
- Dickstein DL, Weaver CM, Luebke JI, Hof PR (2013) Dendritic spine changes associated with normal aging. *Neuroscience* 251: 21–32
- Duran-Aniotz C, Cornejo VH, Espinoza S, Ardiles AO, Medinas DB, Salazar C, Foley A, Gajardo I, Thielen P, Iwawaki T et al (2017) IRE1 signaling exacerbates Alzheimer's disease pathogenesis. *Acta Neuropathol* 134: 489–506
- Duran-Aniotz C, Rivera-Krstulovic C, Poblete N, Ardiles AO, Li Diaz M, Mae C, Sabusap P, Gerakis Y, Miranda FC, Diaz J et al (2022) The unfolded protein response transcription factor XBP1s ameliorates Alzheimer's disease by improving synaptic function and proteostasis. *bioRxiv* <https://doi.org/10.1101/2022.06.21.496869> [PREPRINT]
- Frakes AE, Metcalf MG, Tronnes SU, Bar-Ziv R, Durieux J, Gildea HK, Kandahari N, Monshietehadi S, Dillin A (2020) Four glial cells regulate ER stress resistance and longevity via neuropeptide signaling in *C. elegans*. *Science* 367: 436–440
- Gavilán MP, Vela J, Castaño A, Ramos B, del Río JC, Vitorica J, Ruano D (2006) Cellular environment facilitates protein accumulation in aged rat hippocampus. *Neurobiol Aging* 27: 973–982
- Gibson GE, Peterson C (1987) Calcium and the aging nervous system. *Neurobiol Aging* 8: 329–343
- Go YM, Jones DP (2017) Redox theory of aging: Implications for health and disease. *Clin Sci (Lond)* 131: 1669–1688
- Godin JD, Creppe C, Laguesse S, Nguyen L (2016) Emerging roles for the unfolded protein response in the developing nervous system. *Trends Neurosci* 39: 394–404
- Hafycz JM, Strus E, Naidoo N (2022) Reducing ER stress with chaperone therapy reverses sleep fragmentation and cognitive decline in aged mice. *Aging Cell* 21: e13598
- Hanus C, Ehlers MD (2016) Specialization of biosynthetic membrane trafficking for neuronal form and function. *Curr Opin Neurobiol* 39: 8–16

- Hart CR, Ryan ZC, Pfaffenbach KT, Dasari S, Parvizi M, Lalia AZ, Lanza IR (2019) Attenuated activation of the unfolded protein response following exercise in skeletal muscle of older adults. *Aging (Albany NY)* 11: 7587–7604
- Hayashi A, Kasahara T, Iwamoto K, Ishiwata M, Kametani M, Kakiuchi C, Furuichi T, Kato T (2007) The role of brain-derived neurotrophic factor (BDNF)-induced XBP1 splicing during brain development. *J Biol Chem* 282: 34525–34534
- Hayashi A, Kasahara T, Kametani M, Kato T (2008) Attenuated BDNF-induced upregulation of GABAergic markers in neurons lacking Xbp1. *Biochem Biophys Res Commun* 376: 758–763
- He L, Loika Y, Park Y, Bennett DA, Kellis M, Kulminski AM (2021) Exome-wide age-of-onset analysis reveals exonic variants in ERN1 and SPPL2C associated with Alzheimer's disease. *Transl Psychiatry* 11: 146
- Henis-Korenblit S, Zhang P, Hansen M, McCormick M, Lee SJ, Cary M, Kenyon C (2010) Insulin/IGF-1 signaling mutants reprogram ER stress response regulators to promote longevity. *Proc Natl Acad Sci USA* 107: 9730–9735
- Hetz C (2021) Adapting the proteostasis capacity to sustain brain healthspan. *Cell* 184: 1545–1560
- Hetz C, Saxena S (2017) ER stress and the unfolded protein response in neurodegeneration. *Nat Rev Neurol* 13: 477–491
- Hetz C, Zhang K, Kaufman R (2020) Mechanisms, regulation and functions of the unfolded protein response. *Nat Rev Mol Cell Biol* 21: 421–438
- Hodge K, Ten HS, Hutton L, Lamond AI (2013) Cleaning up the masses: exclusion lists to reduce contamination with HPLC-MS/MS. *J Proteomics* 88: 92–103
- Hughes D, Mallucci GR (2019) The unfolded protein response in neurodegenerative disorders - therapeutic modulation of the PERK pathway. *FEBS J* 286: 342–355
- Hur KY, So JS, Ruda V, Frank-Kamenetsky M, Fitzgerald K, Kotliansky V, Iwawaki T, Glimcher LH, Lee AH (2012) IRE1 $\alpha$  activation protects mice against acetaminophen-induced hepatotoxicity. *J Exp Med* 209: 307–318
- Hussain SG, Ramaiah KV (2007) Reduced eIF2 $\alpha$  phosphorylation and increased proapoptotic proteins in aging. *Biochem Biophys Res Commun* 355: 365–370
- Imanikia S, Sheng M, Castro C, Griffin JL, Taylor RC (2019) XBP-1 remodels lipid metabolism to extend longevity. *Cell Rep* 28: 581–589.e4
- Kang HJ, Kawasawa YI, Cheng F, Zhu Y, Xu X, Li M, Sousa AMM, Pletikos M, Meyer KA, Sedmak G et al (2011) Spatio-temporal transcriptome of the human brain. *Nature* 478: 483–489
- Kennedy BK, Berger SL, Brunet A, Campisi J, Cuervo AM, Epel ES, Franceschi C, Lithgow GJ, Morimoto RI, Pessin JE et al (2014) Geroscience: linking aging to chronic disease. *Cell* 159: 709–713
- Krukowski K, Nolan A, Frias ES, Boone M, Ureta G, Grue K, Paladini MS, Elizarraras E, Delgado L, Bernales S et al (2020) Small molecule cognitive enhancer reverses age-related memory decline in mice. *Elife* 9: 1–22
- Kuleshov MV, Jones MR, Rouillard AD, Fernandez NF, Duan Q, Wang Z, Koplev S, Jenkins SL, Jagodnik KM, Lachmann A et al (2016) Enrichr: a comprehensive gene set enrichment analysis web server 2016 update. *Nucleic Acids Res* 44: W90–W97
- Lee AH, Scapa EF, Cohen DE, Glimcher LH (2008) Regulation of hepatic lipogenesis by the transcription factor XBP1. *Science* 320: 1492–1496
- Lee AH, Heidtman K, Hotamisligil GS, Glimcher LH (2011) Dual and opposing roles of the unfolded protein response regulated by IRE1 $\alpha$  and XBP1 in proinsulin processing and insulin secretion. *Proc Natl Acad Sci USA* 108: 8885–8890
- Leger M, Quideville A, Bouet V, Haelewyn B, Boulouard M, Schumann-Bard P, Freret T (2013) Object recognition test in mice. *Nat Protoc* 8: 2531–2537
- Liu SY, Wang W, Cai ZY, Yao LF, Chen ZW, Wang CY, Zhao B, Li KS (2013) Polymorphism -116C/G of human X-box-binding protein 1 promoter is associated with risk of Alzheimer's disease. *CNS Neurosci Ther* 19: 229–234
- López-Otín C, Blasco MA, Partridge L, Serrano M, Kroemer G (2013) The hallmarks of aging. *Cell* 153: 1194–1217
- Lourenco MV, Clarke JR, Frozza RL, Bomfim TR, Forny-Germano L, Batista AF, Sathler LB, Brito-Moreira J, Amaral OB, Silva CA et al (2013) TNF- $\alpha$  mediates PKR-dependent memory impairment and brain IRS-1 inhibition induced by Alzheimer's  $\beta$ -amyloid oligomers in mice and monkeys. *Cell Metab* 18: 831–843
- Luis NM, Wang L, Ortega M, Deng H, Katewa SD, Li PWL, Karpac J, Jasper H, Kapahi P (2016) Intestinal IRE1 is required for increased triglyceride metabolism and longer lifespan under dietary restriction. *Cell Rep* 17: 1207–1216
- Ma T, Trinh MA, Wexler AJ, Bourbon C, Gatti E, Pierre P, Cavener DR, Klann E (2013) Suppression of eIF2 $\alpha$  kinases alleviates Alzheimer's disease-related plasticity and memory deficits. *Nat Neurosci* 16: 1299–1305
- Martínez G, Vidal RL, Mardones P, Serrano FG, Ardiles AO, Wirth C, Valdés P, Thielen P, Schneider BL, Kerr B et al (2016) Regulation of memory formation by the transcription factor XBP1. *Cell Rep* 14: 1382–1394
- Martínez G, Duran-Aniotz C, Cabral-Miranda F, Vivar JP, Hetz C (2017) Endoplasmic reticulum proteostasis impairment in aging. *Aging Cell* 16: 615–623
- Martínez G, Khatiwada S, Costa-Mattioli M, Hetz C (2018) ER Proteostasis control of neuronal physiology and synaptic function. *Trends Neurosci* 41: 610–624
- Matai L, Sarkar GC, Chamoli M, Malik Y, Kumar SS, Rautela U, Jana NR, Chakraborty K, Mukhopadhyay A (2019) Dietary restriction improves proteostasis and increases life span through endoplasmic reticulum hormesis. *Proc Natl Acad Sci USA* 116: 17383–17392
- Maurel M, Chevet E, Tavernier J, Gerlo S (2014) Getting RIDD of RNA: IRE1 in cell fate regulation. *Trends Biochem Sci* 39: 245–254
- McLaughlin T, Siddiqi M, Wang JJ, Zhang SX (2019) Loss of XBP1 leads to early-onset retinal neurodegeneration in a mouse model of type 1 diabetes. *J Clin Med* 8: 906
- Medinas DB, Rozas P, Traub FM, Woehlbier U, Brown RH, Bosco DA, Hetz C (2018) Endoplasmic reticulum stress leads to accumulation of wild-type SOD1 aggregates associated with sporadic amyotrophic lateral sclerosis. *Proc Natl Acad Sci USA* 115: 8209–8214
- Morimoto RI, Cuervo AM (2014) Proteostasis and the aging proteome in health and disease. *J Gerontol A Biol Sci Med Sci* 69: S33–S38
- Morrison JH, Baxter MG (2012) The ageing cortical synapse: hallmarks and implications for cognitive decline. *Nat Rev Neurosci* 13: 240–250
- Naidoo N, Ferber M, Master M, Zhu Y, Pack AI (2008) Aging impairs the unfolded protein response to sleep deprivation and leads to proapoptotic signaling. *J Neurosci* 28: 6539–6548
- Naidoo N, Zhu J, Zhu Y, Fenik P, Lian J, Galante R, Veasey S (2011) Endoplasmic reticulum stress in wake-active neurons progresses with aging. *Aging Cell* 10: 640–649
- Nakato R, Ohkubo Y, Konishi A, Shibata M, Kaneko Y, Iwawaki T, Nakamura T, Lipton SA, Uehara T (2015) Regulation of the unfolded protein response via S-nitrosylation of sensors of endoplasmic reticulum stress. *Sci Rep* 5: 1–9
- Oliveira MM, Lourenco MV, Longo F, Kasica NP, Yang W, Ureta G, DDP F, PHJ M, Bernales S, Ma T et al (2021) Correction of eIF2-dependent defects in brain protein synthesis, synaptic plasticity, and memory in mouse models of Alzheimer's disease. *Sci Signal* 14: eabc5429

- Perez-Riverol Y, Csordas A, Bai J, Bernal-Llinares M, Hewapathirana S, Kundu DJ, Inuganti A, Griss J, Mayer G, Eisenacher M et al (2019) The PRIDE database and related tools and resources in 2019: Improving support for quantification data. *Nucleic Acids Res* 47: D442–D450
- Plate L, Cooley CB, Chen JJ, Paxman RJ, Gallagher CM, Madoux F, Genereux JC, Dobbs W, Garza D, Spicer TP et al (2016) Small molecule proteostasis regulators that reprogram the ER to reduce extracellular protein aggregation. *Elife* 5: 1–26
- Prell T, Stubendorff B, Le TT, Gaur N, Tadić V, Rödiger A, Witte OW, Grosskreutz J (2019) Reaction to endoplasmic reticulum stress via ATF6 in amyotrophic lateral sclerosis deteriorates with aging. *Front Aging Neurosci* 11: 5
- Ravello CR, Perrinet LU, Escobar MJ, Palacios AG (2019) Speed-selectivity in retinal ganglion cells is sharpened by broad spatial frequency, naturalistic stimuli. *Sci Rep* 9: 1–16
- Zożycka A, Liguz-Leczna M (2017) The space where aging acts: focus on the GABAergic synapse. *Aging Cell* 16: 634–643
- Ryno LM, Genereux JC, Naito T, Morimoto RI, Powers ET, Shoulders MD, Wiseman RL (2014) Characterizing the altered cellular proteome induced by the stress-independent activation of heat shock factor 1. *ACS Chem Biol* 9: 1273–1283
- Saito A, Cai L, Matsuhsa K, Ohtake Y, Kaneko M, Kanemoto S, Asada R, Imaizumi K (2018) Neuronal activity-dependent local activation of dendritic unfolded protein response promotes expression of brain-derived neurotrophic factor in cell soma. *J Neurochem* 144: 35–49
- Schinzel RT, Higuchi-Sanabria R, Shalem O, Moehle EA, Webster BM, Joe L, Bar-Ziv R, Frankino PA, Durieux J, Pender C et al (2019) The hyaluronidase, TMEM2, promotes ER homeostasis and longevity independent of the UPR ER. *Cell* 179: 1306–1318.e18
- Sharma V, Ounallah-Saad H, Chakraborty D, Hleihil M, Sood R, Barrera I, Edry E, Chandran SK, de Leon SBT, Kaphzan H et al (2018) Local inhibition of PERK enhances memory and reverses age-related deterioration of cognitive and neuronal properties. *J Neurosci* 38: 648–658
- Shoji H, Takao K, Hattori S, Miyakawa T (2016) Age-related changes in behavior in C57BL/6J mice from young adulthood to middle age. *Mol Brain* 9: 1–18
- Smith HL, Mallucci GR (2016) The unfolded protein response: mechanisms and therapy of neurodegeneration. *Brain* 139: 2113–2121
- Soto C, Pritzkow S (2018) Protein misfolding, aggregation, and conformational strains in neurodegenerative diseases. *Nat Neurosci* 21: 1332–1340
- Sunyer B, Patil S, Höger H, Lubert G (2007) Barnes maze, a useful task to assess spatial reference memory in the mice. *Nat Protoc* 390: 10–38
- Sutphin GL, Mahoney JM, Sheppard K, Walton DO, Korstanje R (2016) WORMHOLE: novel least diverged ortholog prediction through machine learning. *PLoS Comput Biol* 12: e1005182
- Szklarczyk D, Gable AL, Lyon D, Junge A, Wyder S, Huerta-Cepas J, Simonovic M, Doncheva NT, Morris JH, Bork P et al (2019) STRING v11: protein-protein association networks with increased coverage, supporting functional discovery in genome-wide experimental datasets. *Nucleic Acids Res* 47: D607–D613
- Tang HZ, Yang LM (2015) Activation of the unfolded protein response in aged human lenses. *Mol Med Rep* 12: 389–393
- Taylor RC (2016) Aging and the UPR(ER). *Brain Res* 1648: 588–593
- Taylor RC, Dillin A (2013) XBP-1 is a cell-nonautonomous regulator of stress resistance and longevity. *Cell* 153: 1435–1447
- Taylor RC, Hetz C (2020) Mastering organismal aging through the endoplasmic reticulum proteostasis network. *Aging Cell* 19: e13265
- Trinh MA, Klann E (2013) Translational control by eIF2 $\alpha$  kinases in long-lasting synaptic plasticity and long-term memory. *Neurobiol Learn Mem* 105: 93–99
- Uehara T, Nakamura T, Yao D, Shi ZQ, Gu Z, Ma Y, Masliah E, Nomura Y, Lipton SA (2006) S-nitrosylated protein-disulphide isomerase links protein misfolding to neurodegeneration. *Nature* 441: 513–517
- Valdés P, Mercado C, Vidal RL, Molina C, Parsons G, Court FA, Martínez A, Galleguillos D, Armentano D, Schneider BL et al (2014) Control of dopaminergic neuron survival by the unfolded protein response transcription factor XBP1. *Proc Natl Acad Sci USA* 111: 6804–6809
- Vogel-Ciernia A, Wood MA (2014) Examining object location and object recognition memory in mice. *Curr Protoc Neurosci* 2014: 8.31.1–8.31.17
- Walter P, Ron D (2011) The unfolded protein response: from stress pathway to homeostatic regulation. *Science* 334: 1081–1086
- Wang L, Ryoo HD, Qi Y, Jasper H (2015) PERK limits drosophila lifespan by promoting intestinal stem cell proliferation in response to ER stress. *PLoS Genet* 11: e1005220
- Wingo AP, Dammer EB, Breen MS, Logsdon BA, Duong DM, Troncosco JC, Thambisetty M, Beach TG, Serrano GE, Reiman EM et al (2019) Large-scale proteomic analysis of human brain identifies proteins associated with cognitive trajectory in advanced age. *Nat Commun* 10: 1–14
- World Health Organization (2020) <https://www.oecd-ilibrary.org/docserver/1ad1c42a-en.pdf?expires=1665514359&id-id&accname=ocid54025470&checksum=BD8497578260858BAD36E169F30C1FD8>
- Yang L, Calay ES, Fan J, Arduini A, Kunz RC, Gygi SP, Yalcin A, Fu S, Hotamisligil GS (2015) S-Nitrosylation links obesity-associated inflammation to endoplasmic reticulum dysfunction. *Science* 349: 500–506